Applied Geomatics

Using Structure from Motion for near-real-time analysis of change detection and flood events in the context of flood preparedness: A case study for the Laufer Muehle area at the Aisch river in Germany

--Manuscript Draft--

Manuscript Number:	AGMJ-D-23-00092
Full Title:	Using Structure from Motion for near-real-time analysis of change detection and flood events in the context of flood preparedness: A case study for the Laufer Muehle area at the Aisch river in Germany
Article Type:	Original Paper
Abstract:	Recent flood events (FE) in Germany have shown that the extent and impact of extreme flood events cannot be estimated solely based on numerical models. For analyzing the development of such an event and to develop and implement safety measures more efficiently, additional data must be collected during the event. Within the scope of this research, the possibilities of near-real-time recording using an unmanned aerial vehicle (UAV) and data processing with the Structure from Motion (SfM) method were tested in a case study. Different recording parameter combinations were tested in the Laufer Muehle area on the Aisch river in Germany. The focus of the investigations was the identification of a parameter combination that allows a short recording interval for aerial imagery. Based on these findings, the identification of changes in the study area by comparing multitemporal photography (flood prevention), as well as the recording of flooded areas during a FE should be possible. The accuracy analysis of the different parameter combinations between two point clouds as well as the process of change detection was done by a Multiscale Model to Model Cloud Comparison (M3C2) and including ground control points. As a result, a parameter combination was identified which led to the desired results in the study area. The processes were transformed into fully automated and scripted workflows, allowing the analysis of the processes in the field and near-real-time.

Manuscript

Using Structure from Motion for near-real-time analysis of change detection and flood events in the context of flood preparedness: A case study for the Laufer Muehle area at the Aisch river in Germany

Michael Kögel, M. Eng.

Technische Hochschule Nürnberg Georg Simon Ohm

Institute of Hydraulic Engineering and Water Resources Management

Nuremberg, Germany

ORCID: 0000-0003-0629-3855

michael.koegel@th-nuernberg.de

Prof. Dirk Carstensen, Dr.-Ing. habil.

Technische Hochschule Nürnberg Georg Simon Ohm

Institute of Hydraulic Engineering and Water Resources Management

Nuremberg, Germany

dirk.carstensen@th-nuernberg.de

Abstract

Recent flood events (FE) in Germany have shown that the extent and impact of extreme flood events cannot be estimated solely based on numerical models. For analyzing the development of such an event and to develop and implement safety measures more efficiently, additional data must be collected during the event.

Within the scope of this research, the possibilities of near-real-time recording using an unmanned aerial vehicle (UAV) and data processing with the Structure from Motion (SfM) method were tested in a case study. Different recording parameter combinations were tested in the Laufer Muehle area on the Aisch river in Germany. The focus of the investigations was the identification of a parameter combination that allows a short recording interval for aerial imagery. Based on these findings, the identification of changes in the study area by comparing multitemporal photography (flood prevention), as well as the recording of flooded areas during a FE should be possible. The accuracy analysis of the different parameter combinations between two point clouds as well as the process of change detection was done by a Multiscale Model to Model Cloud Comparison (M3C2) and including ground control points. As a result, a parameter combination was identified which led to the desired results in the study area. The processes were transformed into fully automated and scripted workflows, allowing the analysis of the processes in the field and near-real-time.

Keywords Structure from Motion, flood event, change detection, M3C2, real-time

1 Introduction

In the context of planning flood protection systems, watercourse maintenance, or in situ analysis and investigation of the effects of flood events (FE), it is imperative to have an extensive and detailed basis of data on a large spatial and temporal scale. Reliable data of terrain information (terrestrial and bathymetric), stream gauging station observation sites, vegetation, and built-up areas are necessary to best analyze area-related conditions or to implement these conditions in planning and modeling.

According to the current state of affairs, these surveys are usually carried out based on available surveying databases, which only reflect the condition of the object or area to be surveyed at the time of the survey. For the most part, these surveys record the terrain heights and the building dimensions at a few points that are significant and relevant for the investigations and in a predefined measurement grid. Important information, such as the vegetation, structural condition/damage, and deformations of the foreland of flowing waters as a result of mass transport (erosion, sediment accumulation), is lost in the process. Such information is, however, prerequisite for an adequate implementation of the current condition in flood investigations and for ensuring meaningful results. Usually, it is not possible to collect this data and information quantitatively within the framework of periodical (twice a year) watercourse monitoring.

The flood events at the rivers Aisch and Zenn, the Franconian Rezat, in North Rhine-Westphalia (NRW) and Rhineland-Palatinate (RP), in Bavaria, Thuringia or Saxony in July 2021 have, besides the extreme meteorological and hydrological impact from climate change, illustrated the importance and primary influence of the mentioned factors on the course of FE.

During the FE in Middle Franconia in the period between July 9, 2021 and July 13, 2021, the rivers Aisch, Zenn, and Franconian Rezat overflowed their banks significantly and flooded large parts of the river basins.

The event, which according to current information resembled a hundred-year flood (HQ_{100}), was the cause of extensive flooding in the area of the Aisch river (approx. 30-35 km west of Nuremberg). At the gauging station Markt Bibart, the highest amount of precipitation in the study area was recorded during the event with 88.61 l/m². In the two weeks before, a total of only 47.56 l/m² was measured. Thus, almost twice the amount of precipitation was recorded during the flood event than in total in the two preceding weeks. Despite the widespread flooding, only limited (property) damage was recorded. No information and data were available on the morphological processes (accumulation, erosion) at the time of the investigations, since the technology proposed here could not yet be applied.

Other parts of Germany were affected even more severely by a flood event. After a heavy rain event in the Ahr valley (North Rhine-Westphalia, Rhineland-Palatinate) in the period between July 14 and July 15, 2021, a flash flood occurred and caused enormous damage to property and people.

In the above cases, it is not yet possible to fully clarify all the circumstances, causes, and effects of the events. However, it is likely that the extreme precipitation may not have been fully covered by existing numerical models. Also, there could be an incomplete database (topography and vegetation) and outdated inventory records in the models. Due to changing weather patterns as a result of climate change, the volatility of such events has increased significantly and statistically calculated infrequent FE are occurring more frequently and more pronouncedly.

To be able to implement this information in the long term and sustainably, recurring recordings and investigations are necessary, for example in monitoring using permanent observation points with highly accurate and state-of-the-art surveying methods. In the context of digitalization, new and optimized measurement methods and models are therefore required to record and map relevant information promptly and to transfer it into measures.

Photogrammetric reconstruction with the Structure from Motion method (SfM) is a technique that can be used to map surfaces and objects. Using mathematical operations, it is possible to create a three-dimensional object (for example point cloud (PC), digital surface model (DSM), or digital terrain model (DTM)) based on spatially overlapping photos. This method was first introduced in the 19th century (Meydenbauer 1867). At that time, it was very costly to determine geometric properties based on photos. Now, computers can process a large amount of data in a short time by using appropriate software solutions. Together with tacheometry and 3D laser scanning, these three techniques are mainly used to generate 3D datasets (Triantafyllou et al. 2019).

Photogrammetric reconstruction of objects offers the advantage of extremely realistic visual mapping and the results can be combined and complemented in many ways with other datasets, for example from terrestrial (TLS) or airborne (ALS) laser scanning. Complementary data analysis as well as extensive comparisons of measurement techniques have already been performed in diverse disciplines such as surveying (Mulsow et al. 2019), archaeology (Marín-Buzón et al. 2021), cave surveying (Kögel et al. 2022), and civil engineering (El-Din Fawzy 2019).

Today, extensive and photorealistic survey datasets can be generated using measurement techniques such as 3D laser scanning and photogrammetric reconstruction using the SfM method.

Within the scope of this research, the possibilities of aerial photogrammetry-based long-term surveying of areas at risk from flooding were investigated. The terrain of a defined study area at the Aisch river (Laufer Muehle, see section 2.2) was photogrammetrically surveyed at different times. The surveys were carried out using different combinations of flight parameters. In this way, optimized parameters were determined, by which the terrain can be recorded with low time expenditure (both in the context of the data acquisition and in the post-processing) and adequate accuracy. The parameters were determined by comparison with a high-resolution reference dataset.

Differences (erosion and accumulation, repositioning of objects, vegetation changes) were detected and categorized by intersecting the multitemporal images. The focus of the investigations was to automate the various processes as far as possible so that an analysis can be carried out highly frequently and in near-real-time in the event of flooding.

2 Study area

2.1 Aisch river

The Aisch river is classified as a 1st order water body (Bayerische Staatskanzlei 2010) and originates about 1.25 km south-southeast of Schwebheim (Bayerisches Landesamt für Umwelt 2022a). It has a length of approx. 84.29 km and flows into the Regnitz about 2.1 km south-southeast of Buttenheim. The river basin of the Aisch river covers 1,006.31 km² (Bayerisches Landesamt für Umwelt 2016) and is characterized by a rural pond landscape (Bayerisches Landesamt für Umwelt 2011).

2.2 Laufer Muehle

Due to the size of the Aisch river basin, it was not possible to include the entire area in these investigations. The focus was therefore on surveying a small area (Laufer Muehle), which could be captured by an aerial drone (in this case a quadrocopter) with a time-cost effective manner. The scalability of the investigation results to a larger investigation area is discussed in section 7. The actual possibilities in this context need to be determined in further investigations.

Starting from the origin of the Aisch river the Laufer Muehle is located at 70.6 riv. km. The area is a small village through which the Aisch river runs directly. A weir is located at the western end of the village and a stream gauging station of the Kronach Water Management Office (Bayerisches Landesamt für Umwelt 2022b) is located approx. 90 m from the weir. The location of the study area is illustrated in **Fig. 1**.

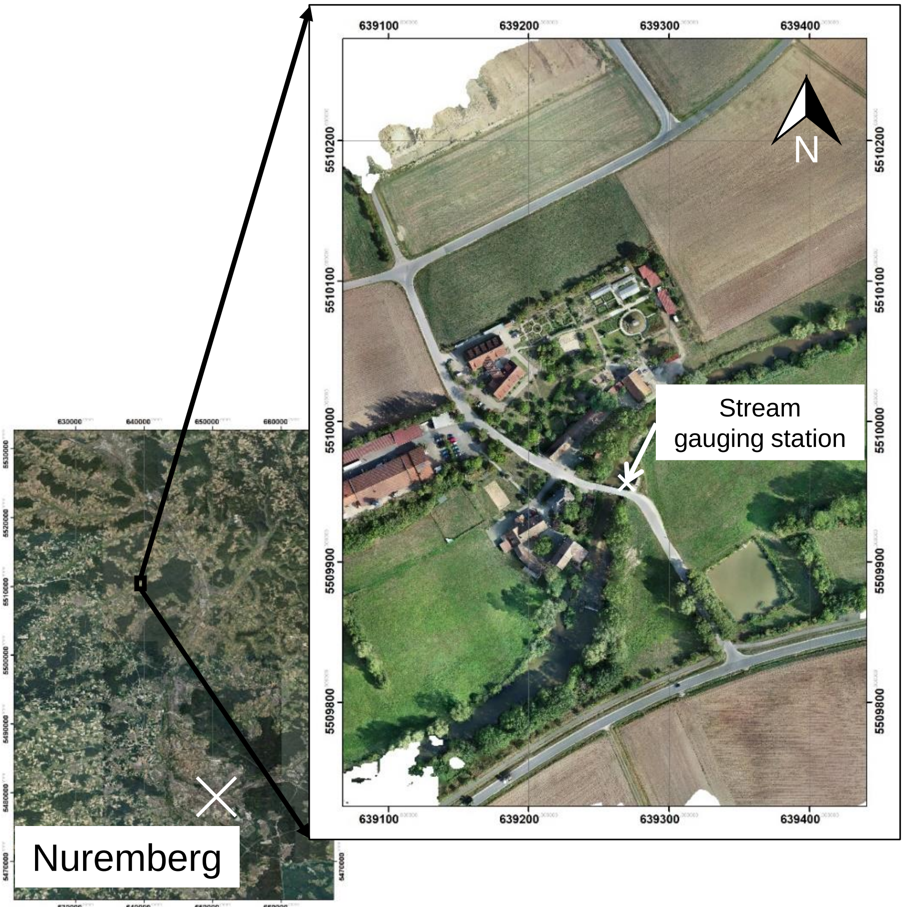

Fig. 1 Location of the Laufer Muehle area and the stream gauging station (source: orthophoto left image: www.geoservices.bayern.de, raster information according to reference system EPSG 25832; orthophoto right image: results from own airborne images)

The area was particularly well suited for the investigations, mainly because it is very much characterized anthropogenic influences. This made the expectation reasonable that changes in the terrain would be detectable between the multitemporal surveys carried out and that these changes would be indentifiable in the different recordings. In addition, this area is regularly affected by flood events, making it likely that the recording methodology described here could be applicable in the event of local flooding.

The water levels of the Aisch river at Laufer Muehle are recorded at the stream gauging station in 15 minute time intervals, which provides good plausibility of survey results. **Table 1** lists the main values of water level and discharge at the Laufer Muehle stream gauging station.

Table 1 Main values of water level and discharge at the Laufer Muehle stream gauging station (Bayerisches Landesamt für Umwelt 2022b)

	main values (1964 – 2012)	main values (1927 - 2012)

	water level [cm]				discharge [m³/s]		
	winter	summer	year		winter	summer	year
LW	170	169	169	**NQ**	0,61	0,30	0,30
MLW	221	211	209	**MLQ**	2,06	1,55	1,47
MW	278	237	258	**MQ**	7,00	3,28	5,13
MHW	453	383	464	**MHQ**	63,30	28,30	70,80
HW	563	548	563	**HQ**	218,00	360,00	360,00

The reporting levels at the Laufer Muehle stream gauging station are given as follows according to Bayerisches Landesamt für Umwelt (2023):

Notification level 1: 400 cm

Small localised outburst floods

Notification level 2: 430 cm

Agricultural and forestry areas flooded or slight traffic obstructions on main roads and municipal roads

Notification level 3: 480 cm

Individual built-up areas or cellars flooded or closure of inter-urban traffic routes or isolated use of water or dam weirs required

Notification level 4: 540 cm

Built-up areas flooded on a large scale or large-scale deployment of water or dam weirs required

2.3 Flood event 2021

As already mentioned in section 1, large-scale flooding in the area of the Aisch resulted from the FE in July 2021. Accordingly, the area of Laufer Mühle was also flooded over a large area. **Fig. 2** shows aerial photographs from this FE and visualizes corresponding discharge and water level parameters.

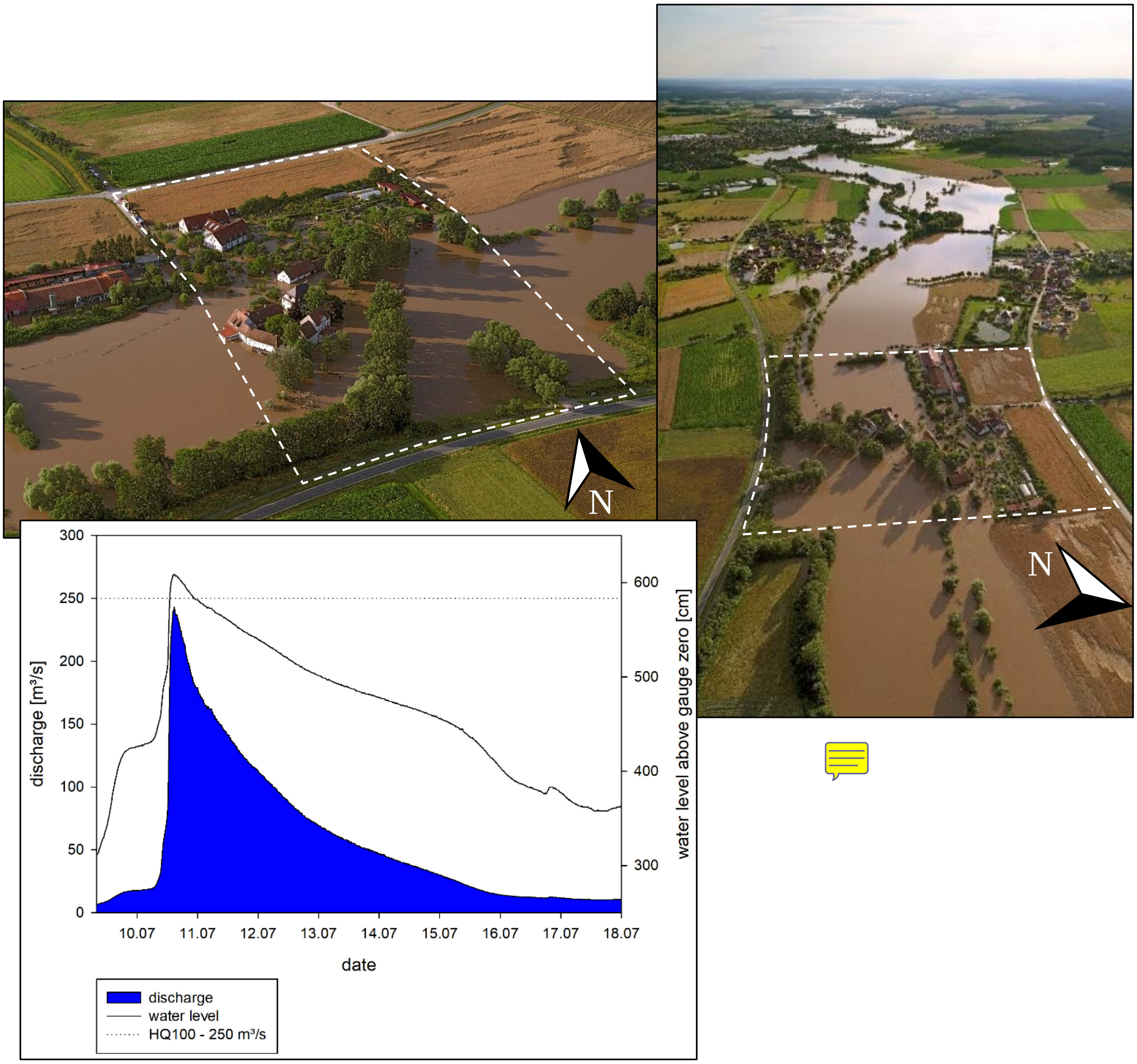

Fig. 2 a) Flooding of the Aisch river on July 12, 2021, in the area of Laufer Muehle with the area of investigation indicated (source of photos: Wasserwirtschaftsamt Nürnberg 2021). b) Discharge and water level at the stream gauging station Laufer Muehle during the flood event in July 2021 with the respective HQ_{100} discharge indicated (Bayerisches Landesamt für Umwelt 2022b)

It is important to note that according to Bayerisches Landesamt für Umwelt (2022b) the stream gauging station starts to become circumferential at a discharge of about 28 m³/s. The validity of the gauge values for Q>28 m³/s can therefore not be evaluated with absolute certainty.

3 Methods

3.1 Measuring device

3.1.1 Data acquisition with unmanned aerial vehicle

An unmanned aerial vehicle (UAV) of the type DJI Phantom 4 RTK was used for data acquisition. The device is equipped with a camera with a 1" CMOS sensor and a resolution of 20 MP and can be operated both manually and autonomously. The autonomous control makes it possible to give the device predefined trajectories, which are subsequently flown independently by the device. Due to the spatial definition of these trajectories, data recordings can be performed again at a later time at approximately the same positions, which makes the potential for comparison and superposition of these multitemporal recordings very high.

Based on the acquired photo data, three-dimensional terrain data was derived by using the SfM post-processing method. The date of the surveys was selected in such a way that the study area was recorded in consideration of high (summer, survey 1) and low (autumn, survey 2) vegetation. In this way, seasonal fluctuations could also be taken into account and represented when detecting changes.

Another way of recording extensive terrain information in three dimensions is by using a laser scanner. With this methodology, the terrain is recorded by an optical light beam. The light beam emitted by the device is reflected by an object and sent back to the measuring device. By comparing the emitted and the received light beam, conclusions can be drawn about the distance of the measuring device to the object, with the distance determination considering the speed of light. For example, a common method for laser-based distance determination is the time-of-flight method or light detection and ranging (LIDAR, Vosselman and Maas 2011).

LIDAR acquisition can be terrestrial (terrestrial laser scanning, TLS) or airborne (airborne laser scanning, ALS). Since photogrammetry and laser scanning are complementary measurement techniques and have applications in many research disciplines, extensive research has already taken place to compare and combine the corresponding datasets (Baltsavias 1999a; Cawood et al. 2017; El-Din Fawzy 2019; Grussenmeyer et al. 2008; Luhmann 2013; Talha and Fritsch 2019; Waele et al. 2018).

Information about and an extensive listing of the technical specifications of commercial ALS units are provided in Baltsavias (1999b). However, it should be mentioned that the systems have developed significantly in recent years and the listing no longer generally reflects the current state of the art. However, the basic features of the recording technique remain mostly the same in their use, which is why this literature reference is mentioned here, despite it perhaps being out-of-date.

3.1.2 GPS-assisted data acquisition

By using global navigation satellite systems (GNSS), such as the Global Positioning System (GPS), it is possible to georeference the data acquired by a UAV and thus assign globally comprehensive coordinate systems. Supplementary satellite positioning services can be used to increase the positional accuracy of this data. The German Satellite Positioning Service (SAPOS) provides a real-time positioning service (high-precision real-time positioning service, HEPS), and by applying the real-time kinematic (RTK) method enables precise position determination with a position accuracy of 1-2 cm and height accuracy of 2-3 cm (SAPOS 2015). The GNSS correction data streams are sent to the instrument via NTRIP (Networked Transport of RTCM via Internet Protocol) over the mobile data network. This type of position determination is now used in diverse measurement devices in both terrestrial (Mancini and Salvini 2020), bathymetric (Xie et al. 2021), and hybrid data acquisition (Kutschera et al. 2018).

This type of positioning was used for both aerial imaging and georeferencing of the GCP (see section 3.1.3).

3.1.3 Using ground control points for georeferencing and plausibility check of measurement data

Reference objects (ground control points, GCP) are often used in connection with three-dimensional data acquisition. These may be different objects which can be used, for example, for georeferencing, accuracy or error determination, and for combining differently recorded data sets. In the course of this research, 13 GCP in the form of flat plates with a coded marking were placed in the survey area during each survey. These were used to validate the SfM results (section 3.3.5) and to generate an optimized reference dataset (dataset M1), which would provide the most accurate results when analyzing changes in the study area and therefore be used as a comparison dataset for further results related to the change detection (CD). The GCP were surveyed using a GNSS rover with RTK connectivity. Except for GCP11, which was intentionally offset by approximately 1 m from the previous survey for accessibility reasons, the GCP in survey 2 were placed at nearly the same position (distance<0.10 m) as in survey 1. **Fig. 3** shows the location of the GCP in the survey area.

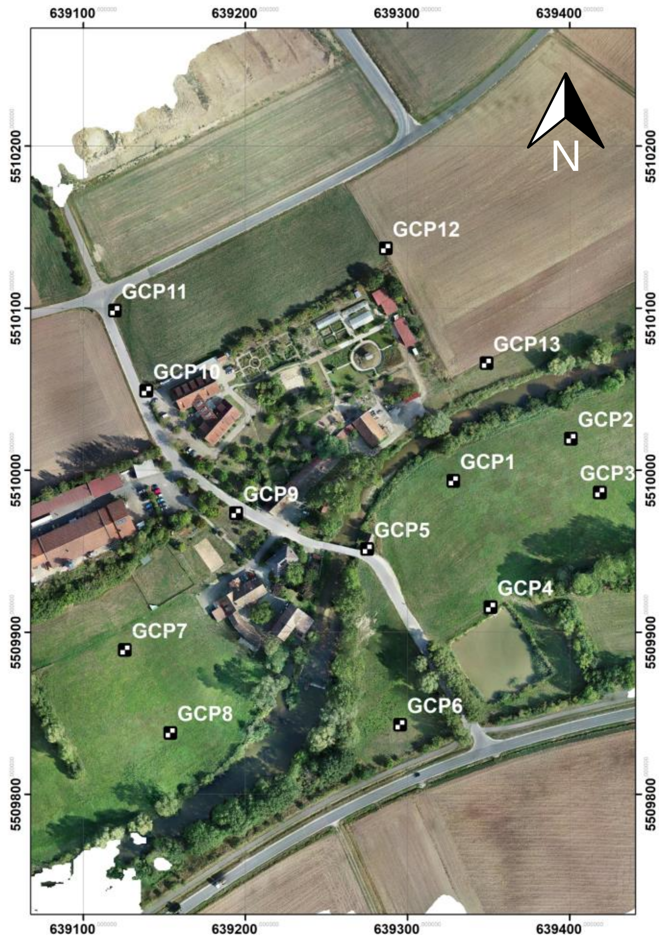

Fig. 3 Location of the georeferenced GCP at surveys 1 and 2 in the study area

The use of GCP usually requires a significant amount of time and is often the largest time commitment associated with photogrammetric acquisition in a study area (Forlani et al. 2018). Also, proper positioning of GCP, especially in the context of terrain survey during a flood event, can be difficult, or only possible at high safety risk. Aware that higher accuracy of the computational results could have been achieved by integrating the GCP into the SfM process, the GCP were therefore primarily used to evaluate the accuracy of the generated PC as well as to generate the optimized reference dataset M1.

An initial assessment of the accuracy of the reconstructed datasets was made by comparing them with the GCP surveyed in the field (sections 3.3.5 and 4.3). **Table 2** shows the positional accuracies of the GCP at surveys 1 and 2.

Table 2 Position accuracy (3D) of the GCP (GNSS rover)

	accuracy [cm]	
Name	**survey 1**	**survey 2**
GCP1	1.36	2.14

GCP2	1.6	2.12
GCP3	1.68	2.41
GCP4	1.52	2.48
GCP5	2.33	2.24
GCP6	1.78	2.72
GCP7	1.5	1.72
GCP8	1.46	1.92
GCP9	1.59	1.81
GCP10	1.53	1.96
GCP11	1.4	2.03
GCP12	1.36	1.6
GCP13	1.65	1.84

It can be seen that, except for GCP5, the accuracy values in survey 1 were constantly better than in survey 2. In principle, a large number of factors can influence the accuracy of GNSS measurements. Especially in the context of the detectability of satellites, which continuously change their position, variations can occur in data acquisitions performed at different points in time. However, the accuracies of all the measurements were within the limits specified in SAPOS (2015).

3.2 Selecting flight and data acquisition parameters

In the context of the concept described here for long-term observation using aerial photogrammetry, the area of the Laufer Muehle was recorded with different parameters. The selection of the parameters was dependent on the desired outcomes:

1. analysis of changes in the study area, both morphological and anthropogenically influenced
2. high-frequency recording during a flood event for the analysis of the development of the flood progression

The basic aim was to ensure the shortest possible processing time for both data acquisition and data processing (post-processing). This should make it possible to make relevant decisions during a flood event in the shortest possible time intervals and to be able to initiate appropriate measures under certain circumstances. Thus, the parameters had to be chosen in a way that the results can be achieved with as little time as possible.

Concerning the identification of multitemporal changes, the geometric aspects of the study area had to be sufficiently represented in all three dimensions. This applied to the results of survey 1 as well as to the comparison states of survey 2.

Recording the vertical component of water is fundamentally difficult for various reasons. Especially under uncontrolled conditions, light refraction effects as well as the constant movement of the water ensure that the photogrammetric evaluation of the image data leads to inaccurate, wrong, or even no results at all. In the context of floodplain assessment, however, the positional components of water can be well derived from orthographic images. Incorporating terrain information enables an approximation of the water depth, from which the vertical component of the water level position can also be estimated.

The relevant flight parameters for the photogrammetric surveys are listed below:

- flight mode (normal grid (NG) / double grid (DG))
- flight altitude
- ground sampling distance (GSD); specifies the size of the image pixel projected into the object space (Eltner et al. 2022)
- flight velocity
- camera tilt
- horizontal overlap
- vertical overlap
- shutter priority

In the case of drone-supported and area-wide recording of a survey area, a distinction is usually made between a simple flight (normal grid) and a cross-flight (double grid). In the normal grid variant, the UAV moves along simple, parallel flight paths, at the end of which a turn maneuver initiates the next flight path. In the case of a double grid flight, the UAV moves along an additional grid rotated by 90°. In this way, more details can be captured and additional photographic perspectives can be obtained, but both the number of images and the duration of the flight are approximately doubled.

The selected flight altitude is decisive for the level of detail with which a survey area is imaged. The resolution (ground sampling distance, GSD, Eltner et al. 2022) with which the surface is imaged results depending on the inner orientation of the camera (section 3.3.1) and the flight altitude. In the case of the used UAV unit, the GSD according to DJI (2023) is given by

$$GSD_{DJI-P4RTK}[cm/Pixel] = \frac{\text{pixel pitch}}{\text{focal length}} \cdot \text{flight altitude} = \frac{h[m]}{36.5} \quad (1)$$

The flight speed during data acquisition is limited by various factors. To avoid blurry and out-of-focus photos, care must be taken to set a camera exposure time that is short or appropriate for the flight speed. Thus, in low light conditions and at too low flight altitudes, certain flight speeds cannot be exceeded without a loss of accuracy in the photos. By setting a priority for the camera's shutter speed (shutter priority), other imaging parameters, such as flight speed, can be adjusted accordingly.

For photogrammetric computation processes, it is generally necessary that an object or terrain is mapped by overlapping photos. The degree of vertical overlap does not influence the duration of a single mission, since this setting only determines when and at which distance along the flight path a photo is taken. Thus, with a higher vertical overlap, more photos are taken, which results in a higher post-processing time. However, the flight duration remains unaffected.

This differs for horizontal overlap. An increase in the percentage overlap results in an increase in the individual trajectories and hence in the duration of a mission. For example, an increase in the horizontal overlap from 60% to 80% leads to a doubling of the number of images.

Concerning the mentioned parameters, different flights (missions) were carried out, taking into account varying flight parameters. This enabled the determination of the minimum necessary parameters to carry out the planned analyses while maintaining high accuracy. A total of 16 different parameter constellations (M2-M17) were investigated. Based on findings from past investigations, the parameters for M2 were chosen (low flight altitude and DG-flight mode) in such a way that the data set with the highest accuracy would most likely result from this flight. To further optimize the results of M2, a second processing of these data was performed considering GCP within the SfM process, resulting in the reference data set M1, which was used for the accuracy analysis of M2-M17. This made it possible to determine the effect and intensity of each parameter on the accuracy of the reconstructed geometries. **Table 3** shows the flight parameters used in the performed flights as well as the required flight duration (specified by the flight software) and the resulting number of images.

Table 3 Flight parameters of the missions M1-M17 with M1 optimized with GCP. High values (flight duration, number of images) are gray colored

mission	flight mode	flight altitude [m]	GSD [cm/Pixel]	flight velocity [m/s]	camera tilt [°]	horizontal overlap [%]	vertical overlap [%]	shutter priority [s]	flight duration [min]	number of images [-]
M1	DG	50	1.37	3	60	60	80	no	51:45	950
M2	DG	50	1.37	3	60	60	80	no	51:45	950
M3	NG	50	1.37	3	60	60	80	no	29:14	536
M4	DG	80	2.19	4	60	60	80	no	21:58	337
M5	NG	80	2.19	4	60	60	80	no	14:00	214
M6	DG	110	3.01	4	60	80	80	no	21:04	244
M7	DG	110	3.01	4	60	60	80	no	15:20	173
M8	NG	110	3.01	4	60	60	80	no	10:05	112
M9	DG	110	3.01	4	90	60	80	no	10:50	122
M10	DG	110	3.01	8	60	60	80	1/1600	08:08	173
M11	NG	110	3.01	8	60	60	60	1/1600	05:18	58
M12	NG	110	3.01	4	90	60	80	no	09:54	110
M13	DG	110	3.01	8	90	60	80	1/1600	05:48	122
M14	NG	110	3.01	8	90	60	60	1/1600	05:10	57
M15	DG	110	3.01	4	90	60	60	no	10:44	64
M16	NG	110	3.01	4	60	60	60	no	10:04	59
M17	DG	110	3.01	4	60	60	60	no	15:24	90

3.3 Data processing

Photogrammetry generally describes the method of determining the spatial position and three-dimensional shape of an object or an area by superimposing several photos taken from different perspectives. The aim is to obtain height and position information about the respective observation area by evaluating the photos. This contrasts with the image acquisition method, in which the three-dimensional geometry of a body is converted into a two-dimensional image.

For the photogrammetric computation of a three-dimensional point cloud (PC) using the SfM method, a variety of software applications exist, which differ greatly in their functions, compatibilities, costs, and applications. For example, OpenDroneMap (OpenDroneMap 2022) is an application that is provided free of charge and can therefore be used by a wide range of users. In the context of this research, the application Agisoft Metashape (formerly PhotoScan) (Agisoft LLC 2022a) was used, because extensive experience in its use was available, especially from previous research. In addition, the software offers different interfaces, for example with the Python programming language (Agisoft LLC 2022b), which allows automated processing procedures by script execution. In terms of long-term observation, this offers great potential, as optimized comparison and analysis processes can be applied quickly and in a targeted manner.

The basic principle of photogrammetry, namely 3D reconstruction based on overlapping photo images, is explained for example in Eltner et al. (2022), Wiggenhagen and Steensen (2021) and Luhmann (2018).

According to Eltner et al. (2022), the photogrammetric workflow can be divided into the three main steps of

- image orientation,
- point cloud extraction and surface modeling, and
- orthophoto generation,

which are explained in their main features in the following. Since the last two points are post-processing products resulting from the reconstruction process, they will be summarized.

The principle of the pinhole camera describes the mathematical relationship between the 3D coordinates of a point in object space and its projection on an image plane (Eltner et al. 2022). Starting from a projection center, a point in the object space as well as its projection on the photo are located along the same imaginary line, which makes them collinear. This relationship can be represented mathematically by the collinearity equations (Eq. (2)) and represents the basis of photogrammetric dimension determination.

$$
\begin{aligned}
x &= -c \cdot \frac{r_{11} \cdot (U - U_0) + r_{12} \cdot (V - V_0) + r_{13} \cdot (W - W_0)}{r_{31} \cdot (U - U_0) + r_{32} \cdot (V - V_0) + r_{33} \cdot (W - W_0)} + x_{pp} \\
y &= -c \cdot \frac{r_{21} \cdot (U - U_0) + r_{22} \cdot (V - V_0) + r_{23} \cdot (W - W_0)}{r_{31} \cdot (U - U_0) + r_{32} \cdot (V - V_0) + r_{33} \cdot (W - W_0)} + y_{pp}
\end{aligned}
\tag{2}
$$

where

- x and y are the image coordinates in the camera system

- U, V, W are the object coordinates of a point

- c, x_{pp}, and y_{pp} are parameters of the inner orientation of the camera; respectively focal length and coordinates of the principal point

- r_{11}, r_{12}, r_{13}, r_{21}, r_{22}, r_{23}, r_{31}, r_{32}, r_{33} are elements of a rotation matrix and are determined by the three rotation angles omega, kappa, phi, which describe the rotation around W, V, and U

- U_0, V_0, W_0 are the coordinates of the image projection center in the object coordinate system

However, the projection of a 3D object point onto a 2D image plane results in an infinitely long image beam on which the point is potentially located and as a result, its position in the object space cannot be identified. For this reason, for the photogrammetric determination of object coordinates, the object to be determined is imaged from at least two different positions/perspectives (stereo-pair images). By the intersection (forward intersection) of several such spatial beams, the 3D coordinates of an object can be unambiguously defined by determining the image orientation. A PC is created from a large number of such coordinate determinations, which, depending on the quality and density, represents an object in greater or lesser detail.

Based on this data, further data sets can be generated, for example, orthophotos, which are often used in GIS applications for visualization and localization of georeferenced measurement data. Interpolation methods and various mesh algorithms can be used to condense point cloud data sets that have been calculated, which provides an area-wide representation of the terrain.

Using aerial photogrammetry, large viewing areas can be captured photographically in a relatively short time. The accuracy as well as the extent and resolution of these data depend significantly on

- the extent of the terrain,
- the flight parameters (flight altitude, overlap of the photo images, etc.; see in section 3.2),
- the quality of the position determination (for example by GNSS),
- the position accuracy of (if used) reference objects (GCP), and
- the selected processing parameters during photogrammetric processing,

which are to be chosen according to the desired results. However, survey areas usually differ in their characteristics from each other and the acquisition conditions (for example, resulting from weather conditions) can lead to different calculation results despite the same acquisition and processing parameters during PC generation.

Thus, measuring the quality of terrain models is a complex task due to the large number of variables involved (Forlani et al. 2018) and the additional dependence of the quality of the results on the conditions of the different study areas. Accordingly, a generally valid statement considering all relevant aspects mentioned in section 3.2 cannot be given by a single study (Forlani et al. 2018).

Thus, the appropriate study parameters must always be adapted based on the study area. An approach to analyzing the accuracy of computational results from aerial surveys with different survey parameters is given in Mora-Felix et al. (2020). Accuracy studies on the quality of the DJI Phantom 4 RTK GNSS system were performed in Przybilla and Bäumker (2020).

3.3.1 Camera calibration.

To avoid different distortion effects, resulting for example from the curvature of the camera lens, it is necessary to calibrate corresponding camera parameters. Usually, these are the following parameters:

- f - focal length (in pixels)
- x_{pp}, y_{pp} (in Agisoft Metashape c_x, c_y) - coordinates of the principal point (in pixels)
- b1, b2 - affinity and non-orthogonality coefficients (in pixels)
- k1, k2, k3, k4 - radial distortion coefficients (dimensionless)
- p1, p2 - Tangential distortion coefficients (dimensionless).

Calibration can be performed, among other things, by recording GCP positioned with high accuracy. By recording and comparing them with the SfM calculation results, the accuracy of the parameters can be estimated and an appropriate correction can be made. Furthermore, bundle block adjustment with self-calibration is described in Wiggenhagen and Steensen (2021), through which appropriate adjustments can be made.

In the SfM process with Agisoft Metashape, a pre-calibration with initial values is performed at the beginning of the processing. In the context of the align photos process as well as by using GCP, the camera alignment can be optimized and the above-mentioned parameters can be calibrated.

In the context of these investigations (except for the reference data set M1, which was optimized using GCP), the camera was calibrated only based on the align photos process (M2-M17).

3.3.2 Determination of the SfM parameters and the processing sequence

As already explained in section 3.2, a variety of factors during data acquisition influence the photogrammetric work scope, the data accuracy as well as the duration of this process. Likewise, the computational parameters in the SfM process in conjunction with the mentioned factors affect the reconstructed 3D PC. Due to a large number of factors, it was decided in these investigations to use parameters that have led to good results in past investigations. It cannot be excluded that optimization of these parameters can lead to an improvement of the results, or that a reduction of the accuracies of the individual parameters leads to an insignificant change in the imaging accuracy of the calculation results, which, however, can lead to significantly shorter processing times and thus possibly to an even better implementation of the investigations. This aspect will be discussed again in section 7.

Based on findings from past studies, the downscale parameter was set to 2 (Medium) when aligning the photos (matchPhotos) and to 2 (High) when generating the depth images (buildDepthMaps). This factor describes the scaling of the photos in the SfM process and specifies whether an image is used in full resolution (downscale=0) or reduced form (downscale≥1). The respective parameters are listed below according to Agisoft LLC (2022a):

Table 4 Downscale parameter in the matchPhotos and buildDepthMaps processes (Python)

matchPhotos - downscale	**buildDepthMaps - downscale**
Highest = 0	Ultra = 1
High = 1	High = 2
Medium = 2	Medium = 4
Low = 4	Low = 8
Lowest = 8	Lowest = 16

When selecting a lower resolution level, the photo is scaled up by a factor of 4 per grading, compared to the setting without downscaling. When the highest resolution level is selected, the photo is scaled up by a factor of 4. A high degree of accuracy results in principle in a higher accuracy of the calculation results, but also in a significant increase of the time needed for data processing as well as in a higher number of points of the resulting PC (Agisoft LLC 2022a).

During the analysis of the photos, key points (KP) are determined on each photo. These are points that represent salient features in a photo. If such points are identified on several images, a relationship between these images can be established based on the resulting tie points (TP).

By a gradual selection of TP based on different threshold values, point filtering can already take place during the SfM process. Filtering was performed following TP generation with default parameters according to Agisoft LLC (2022a), with camera position optimized after each of the filtering steps:

- Reprojection error = 0.5
- Reconstruction uncertainty = 10
- Image count = 2
- Projection accuracy = 10

The choice of the correct parameters always depends on the study area as well as the chosen acquisition parameters and can therefore hardly be defined in a general way.

As a result of the SfM process, a dense point cloud (PC) was generated and exported for each of the performed missions, among other data sets. The PC were used for the localization and identification of changes (CD) in the study area.

During the SfM process, a confidence value was calculated for each point of a PC, which, based on the selected settings, reflects how reliably a point represents reality. The confidence values were between 1 and 255, with 1 indicating very low confidence and vice versa. By filtering values with a low confidence value, it stands to reason that erroneous values can be filtered, thereby achieving a reduction in the error-proneness of each data set and mitigation of noise.

For each of the PC from each mission, each of which differed in their acquisition parameters, the filtering results varied widely as a result of different confidence values, so it was not possible to make a consistent statement by choosing a general confidence value. However, it was assumed that at least filtering the points with the lowest mapping accuracy (confidence value = 1) would lead to a significant improvement in the reconstruction results. The following analyses were therefore conducted on the unfiltered and the filtered point cloud.

3.3.3 Three-dimensional comparison of multitemporal terrain data sets - M3C2

By comparing measurement data sets in the context of long-term observations, temporal differences in the surface structure in a study area can be determined. The high density of measurement points (with possible point distances in the low single-digit centimeter range), which can be achieved by photogrammetric processing, allows high accuracy in the estimation of change.

The presence of vegetation and seasonal effects for CD analysis, both between data sets from data acquisitions close in time and far apart in time, significantly complicates the proper categorization of distance determination. Influenced by weather, short-term movements of vegetation (leaves, branches) can occur even during a single data acquisition process, leading to errors in the SfM process. In the long term, additional seasonal effects (vegetation growth and shrinkage, snow accumulation) can occur (Qin et al. 2016). Such change is usually not part of the desired change analysis, but can sometimes lead to significant distance differences between multitemporal datasets.

In the course of the investigations presented here, the aim was to determine differences or discrepancies between multitemporal photos. Since important comparative data would be neutralized in the course of data filtering, the investigation was conducted with the aim of comparing largely unfiltered data sets and the data filtering was primarily related to scattering points (noise). Especially in connection with the presence of vegetation, however, this resulted in difficulties in distinguishing between constructive or terrain-specific changes and vegetation changes caused by seasonal effects (see section 4.4).

Since the localization of the measurement points at the same location is impossible with multitemporal measurement data recordings, it is necessary to model the terrain locally for the distance comparison. The problem of distance comparison based on measurement points with different localities is visualized in **Fig. 4**. If point data sets are compared by direct point comparison (Fig. 4, A) by using the closest point method, this can lead to a misestimation in determining distance because the equivalent measurement point with the same locality was not mapped in the comparison dataset. In addition, this method is susceptible to measurement data noise, since fluctuations in the data sets are not normalized and points with a high error potential are used directly for distance determination. By locally modeling a surface (Fig. 4, B, and C) based on one of the two PC, an approximation to the terrain surface and thus to the actual distance determination can be made.

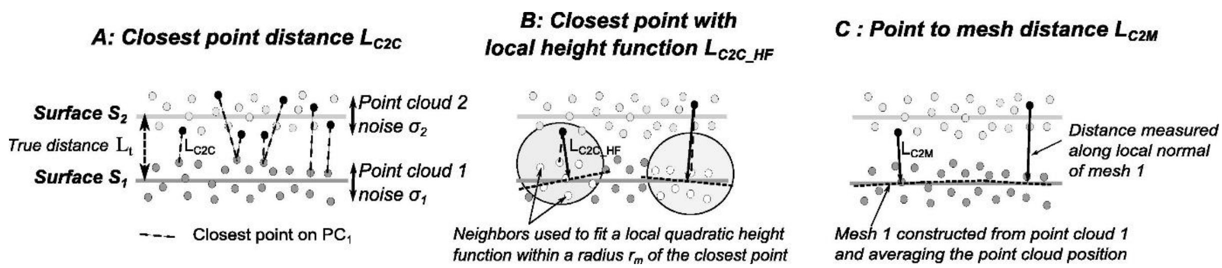

Fig. 4 Existing 3D comparison methods between two PC (Lague et al. 2013).

A goal-oriented application for distance determination between two PC datasets is provided by the comparison through the Multiscale Model to Model Cloud Comparison (M3C2) method. It is described in Lague et al. (2013) and Winiwarter et al. (2021), among others, and is characterized in particular by the fact that it

- determines the distance directly through the PC, without meshing or gridding,

- determines the local distance between two PC along the normal surface direction, which tracks the 3D variations in surface orientation,

- generates a confidence interval for each distance measurement depending on the roughness of the PC and the registration error.

In this method, the orientation of a single point (normal) is calculated based on adjacent points within a region of diameter D (normal scale). Parallel to the normal, a cylinder with height (max depth) and diameter d (projection scale) is generated with the center at the selected point. Within this cylinder, points are defined in the PC to be compared and averaged for the difference determination. This approach does not limit the distance determination to the perpendicular distance between two data sets, or even to the comparison of the nearest points (nearest neighbor), but can be directly related to the terrain morphology.

When calculating the normal, particular attention must be paid to the parameters of the neighboring points to be considered. Choosing diameters that are too small can lead to an overestimation of roughness, which can significantly overestimate the normal (**Fig. 5**, b).

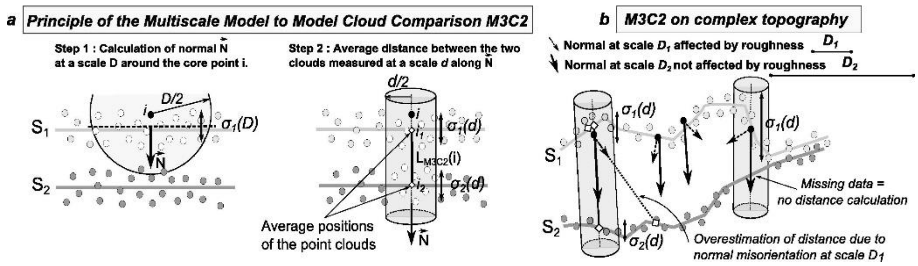

Fig. 5 Description of the M3C2 algorithm and user-defined parameters D (normal scale) and d (projection scale) (Lague et al. 2013).

Extensive research on the accuracies and procedures of different distance determination methods in the context of change detection (CD) is done in Qin et al. (2016) and James et al. (2017) among others.

3.3.4 M3C2: Sensitivity analysis to determine appropriate parameters for distance computation between M2-17 and M1

A general determination of suitable parameters for CD identification is hardly possible due to the different conditions of the study areas and the different issues that arise. Therefore, to determine suitable parameters, a sensitivity analysis was performed in the context of M3C2 distance determination in this study.

The investigation aimed to determine parameters that reflect the difference between two PC to be compared with the smallest possible error. For this purpose, the PC from M1 was chosen as the reference object, since it had the highest accuracy due to the implementation of the GCP into the SfM process (see section 4.3). The PC from survey M16 was chosen as the comparison data set since the comparatively small number of images allowed the time-efficient comparison of many different parameter variants and the comparison with the surveyed GCP suggested a presumably sufficient positional accuracy of the PC (**Fig. 8**).

As a result of the 3D reconstruction by SfM, the normal for each measuring point was already determined in this process, which is why their calculation based on the diameter D (normal scale) was omitted in the M3C2 distance determination. Accordingly, the two parameters remaining for the sensitivity analysis were

- max depth and
- projection scale (d).

Two different observations were carried out, in each of which, concerning a baseline value, one of the two parameters was varied and the other parameter was assumed to be constant.

In the original planning, the analysis was to be based on a suitably defined combination of parameters (max depth = 7.5 m; projection scale = 1.1283 m, with $A=r^2\pi$ corresponding to an area of 1.0 m²), which were to be both increased and decreased by two equal intervals. During the investigations, it turned out that the influence of the respective parameter change did not affect the error development linearly, but rather expressed an exponential influence. With an increase of the values the development of the results was not foreseeable on basis of these limited investigation intervals. Therefore, additional investigation intervals were added.

When analyzing the effect of the max depth parameter on the calculation result, it was varied in an interval of Δ=+/- 2.5 m and ranged from 2.5 m to 25.0 m (with projection scale = constant = 1.1283 m). When analyzing the effect of the projection scale parameter, the interval was defined by Δ=+/- 0.25 m ranging from 0.6283 m to 2.8783 m (with max depth = constant = 7.5 m). Table 4 1 lists the individual investigation variants (case).

Table 5 Parameter combinations (case) of the sensitivity analysis within the M3C2 investigations.

case	projection scale [m]	max depth [m]	case	projection scale [m]	max depth [m]
1	1.1283	2.5	**11**	0.6283	7.5
2	1.1283	5	**12**	0.8783	7.5
3	1.1283	7.5	**13**	1.1283	7.5
4	1.1283	10	**14**	1.3783	7.5
5	1.1283	12.5	**15**	1.6283	7.5
6	1.1283	15	**16**	1.8783	7.5
7	1.1283	17.5	**17**	2.1283	7.5
8	1.1283	20	**18**	2.3783	7.5
9	1.1283	22.5	**19**	2.6283	7.5
10	1.1283	25	**20**	2.8783	7.5

Based on the sensitivity analysis, a preferred variant of the M3C2 parameter combination (case 21) was developed, which was used for the subsequent distance comparisons. The results of this analysis and the parameters of the preferred constellation are explained in section 4.2 and discussed in section 5.2.

3.3.5 M3C2: Parameter selection for distance comparison between M2-M17 and georeferenced GCP

A first assessment of the accuracy of the M2-M17 calculation results could be achieved by comparing them with the GCP placed in the field. Unlike the M3C2 distance determination between the point clouds of different missions, no information about the orientation (normal) was available in the case of the GCP point data. The GCP were placed in the terrain exclusively on flat surfaces, therefore the roughness effects had hardly any influence on the result of the distance comparison if the projection scale (d) was chosen. As the GCP positions were not expected to be subject to major changes in the terrain, which could be verified by comparing the GNSS rover's position values on site between survey 1 and survey 2, the parameter max depth was chosen deliberately small. For this reason, as well as based on the previous statements regarding the parameter selection for projection scale and max depth, in this comparison, the distance determination was carried out only based on the vertical distance of the GCP to the respective comparison point cloud of the individual missions. For this reason, the parameter for normal scale did not have to be selected.

For the M3C2 distance determination, the corresponding parameters were chosen as follows:

- max depth = 1.0 m
- projection scale (d) = 1.0 m

3.3.6 M3C2: Accuracy analysis of data sets M2-M17 by comparison with data set M1

To determine the accuracy of the SfM calculation results of M2-M17, M3C2 distance computation was performed in each case using the parameters determined and optimized in the sensitivity analysis (section 4.2), for both the unfiltered and the filtered data sets.

The comparison was performed in each case by determining a normal distribution function based on the determined distances of each measurement point. In this way, the distribution of the calculated distances could be displayed and the mean value of the deviations between the data sets could be determined. In addition, the standard deviation and the root mean square (RMS) were determined, which indicate the deviation of the data from the mean value and allow statements to be made about the dispersion of the data.

3.3.7 Change detection

According to Dinkel et al. (2020), the change detection (CD) process can be divided into three main steps:

1. co-registration
2. noise detection
3. detection of significant changes

In co-registration, two data sets (for example two PC) are aligned with each other. A common method is the application of an iterative closest point algorithm (Fischler and Bolles 1981), in which a point cloud is iteratively aligned to a reference dataset. In Rusinkiewicz and Levoy (2001) different methods and variants of such algorithms are explained.

While co-registration can significantly improve results from the SfM process (Nota et al. 2022), it can degrade CD results in some circumstances (Lague et al. 2013). Because the purpose of these studies was to investigate the potential for detecting CD using different flight parameter constellations, independent of optimizations using external data sets, the potential for optimization using co-registration processes was not investigatedat this time.

Detection of differences in multitemporal imagery can be performed in two (photographic imagery) or three dimensions (geometric datasets, PC, DTM, etc.). The basic differences between the two methods according to Qin et al. (2016) are explained in **Table 6**.

Table 6 Overview of differences between 2D and 3D CD (Qin et al. (2016)

	2D CD	3D CD
Data sources	• 2D panchromatic/spectral images, 2D vector data	• 3D point clouds, digital surface models, stereo images, multi-view images, 3D models, etc.
Application scale	• Generally applied to LTMR images at a landscape level • Limited applications in very high resolution at individual building level	• Generally applicable to data with any resolution • Applicable for data from oblique views
Advantages	• Well-investigated • Easy to collect data • Easy to implement	• Height component robust to illumination differences • Free of perspective effect even for VHR data • Provide volumetric differences
Disadvantages	• Strongly affected by illumination and atmospheric conditions • Limited by viewing angles, perspective distortions	• Unreliable 3D information may result in artifacts • Partly still expensive data sources

In a 2D data comparison, statements about the height vector and thus the volumetric information of change detection are only possible to a limited extent. In addition, terrain changes below cover, for example in the form of vegetation cover by tree canopies, cannot be detected by two-dimensional nadir images. Since these changes also need to be detected, as well as for the previous reason, 3D analysis was chosen for these investigations.

The occurrence of noise in PC data sets, as the presence of scatter points, can lead to a misinterpretation of the results in the context of CD. Since the points resulting from noise will most likely not be present in the data sets of a time-shifted recording, this is considered a change in the study area, although this leads to a misinterpretation. Especially vegetation and other easily movable objects increase the generation of noise because their movement can cause minimal changes even during a running recording, which are interpreted by the system as actual measurements.

There are different approaches for identifying and filtering these data, which, among other things, take into account the inaccuracies that occur during the analysis processes and explicitly use them as limiting parameters for the analysis. As the goal of these analyses was to identify significant changes (assumption: significant change when -0.25 m≤d≤0.25 m with d being the distance between two multitemporal data sets), measurement points with M3C2 differences within the interval were removed from the data sets.

3.4 Processing sequence for the identification of CD in the area of Laufer Muehle

Fig. 6 illustrates the workflow (data acquisition and processing) described in the previous sections.

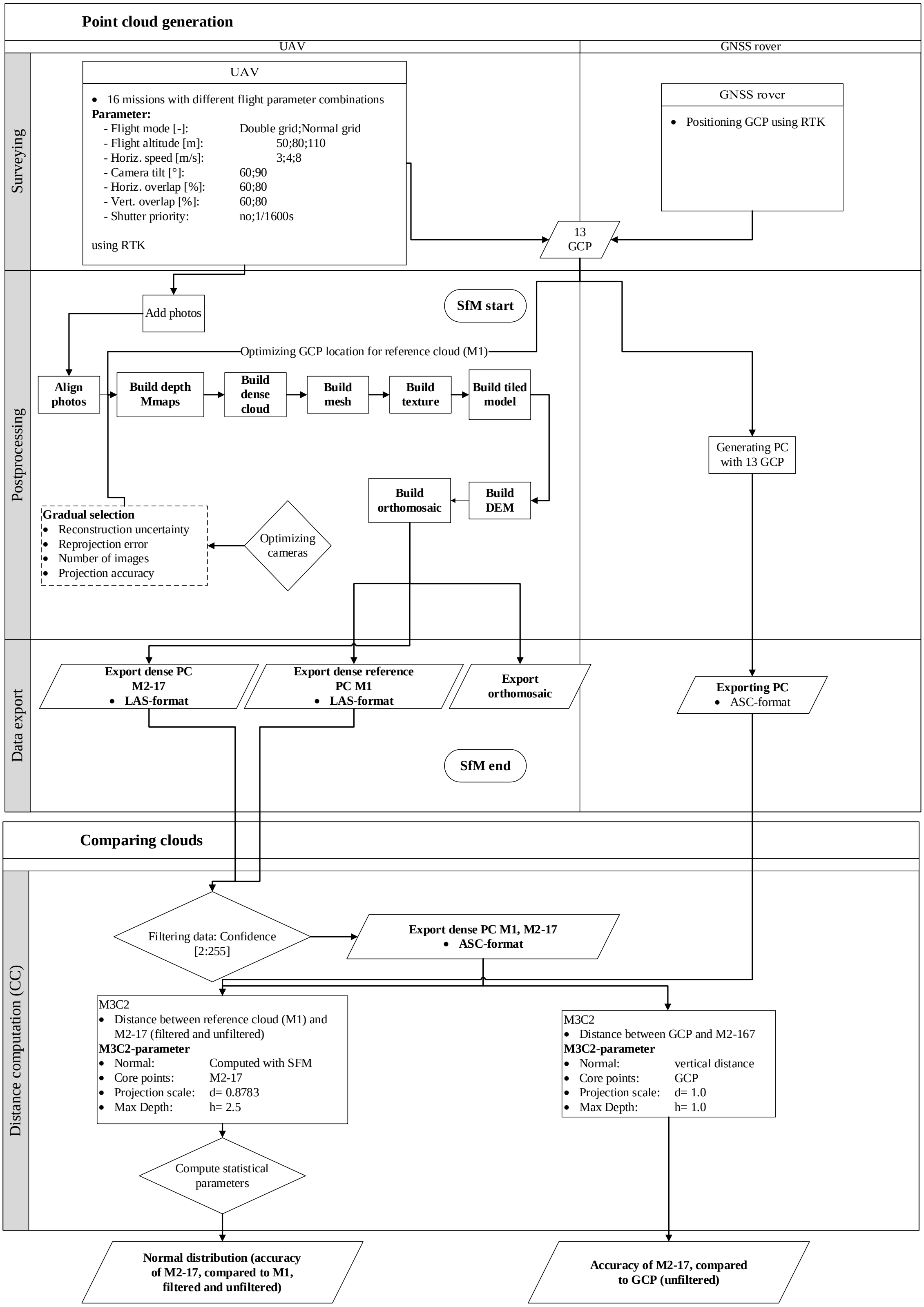

Fig. 6 Processing sequence in distance determination between reference datasets (M1 and GCP) and M2-M17 to determine the accuracy of datasets from missions with different acquisition parameters

4 Results

4.1 3D reconstruction with SfM

As a result of the 3D reconstruction, an unfiltered and a filtered (using confidence value as a filtering parameter, see section 3.3.2) dense PC were available for each of the conducted missions. **Table 7** shows the point counts (unfiltered and filtered), the percentage of filtered points to total unfiltered point counts, and the point difference between surveys 1 and 2 for each of the respective missions.

Table 7 Number of points of the PC from the SfM process, unfiltered and filtered (using confidence value), as well as an indication of the percentage filtered and the point differences between surveys 1 and 2

	survey 1			survey 2				
mission	points unfiltered [10^6]	points filtered (confidence) [10^6]	filtered [%]	points unfiltered [10^6]	points filtered (confidence) [10^6]	filtered [%]	Δpoints: survey1-survey2_unfiltered [%]	Δpoints: survey1-survey2_filtered [%]
M1	349.1	273.0	21.8	290.8	245.6	15.5	16.7	10.0
M2	339.7	267.8	21.2	290.0	244.1	15.8	14.6	8.8
M3	248.5	206.7	16.9	219.4	188.0	14.3	11.7	9.0
M4	152.8	123.4	19.2	104.1	83.3	20.0	31.8	32.5
M5	112.2	94.3	16.0	102.4	87.5	14.5	8.8	7.2
M6	90.4	76.0	15.9	81.9	69.4	15.3	9.5	8.8
M7	94.6	77.6	17.9	85.7	70.7	17.6	9.3	9.0
M8	68.4	58.5	14.5	61.2	52.1	14.8	10.6	10.9
M9	63.9	53.7	16.0	56.4	48.0	14.9	11.8	10.6
M10	92.2	73.4	20.4	58.3	35.3	39.6	36.8	52.0
M11	54.3	43.7	19.5	24.2	11.0	54.5	55.5	74.9
M12	77.8	66.3	14.8	72.6	61.1	15.8	6.8	7.9
M13	63.2	51.5	18.5	36.2	20.1	44.5	42.7	61.0
M14	61.4	49.9	18.7	22.4	9.7	56.5	63.6	80.5
M15	51.0	42.5	16.6	47.2	39.4	16.5	7.3	7.3
M16	54.5	46.0	15.5	53.1	43.9	17.2	2.6	4.6
M17	79.8	64.5	19.1	75.3	60.7	19.4	5.7	6.0

4.2 M3C2: Sensitivity analysis of the parameters used to calculate differences between M2-M17 and the reference data set M1

Fig. 7 presents the results from the M3C2 sensitivity analysis. **Table 8** shows the final parameters from the sensitivity analysis (case 21) as well as the corresponding calculation results when comparing the distance between the reference PC from survey M1 and the PC from survey M16.

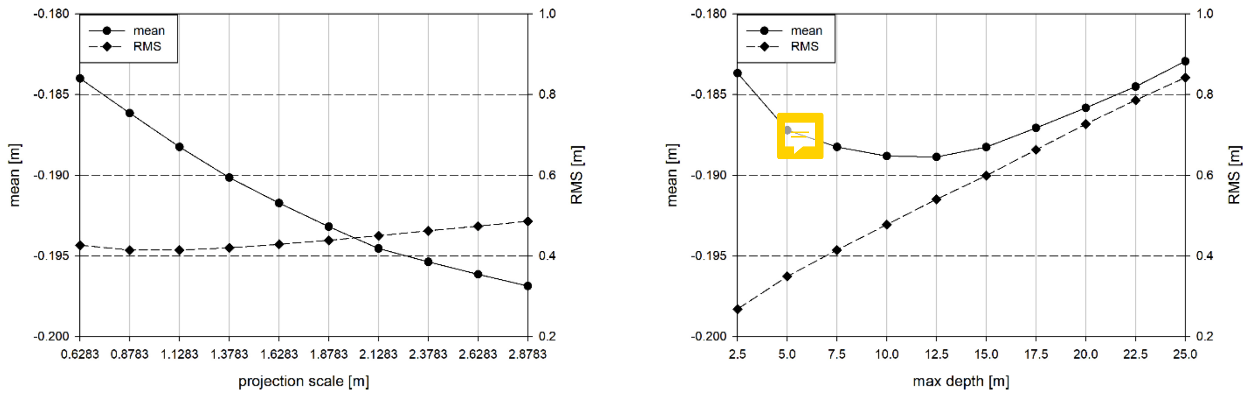

Fig. 7 Development of the RMS as a function of the projection scale (max depth = constant, left) and as a function of max depth (projection scale = constant, right) in the context of the M3C2 sensitivity analysis.

Table 8 Optimized parameters (case 21) developed from the sensitivity analysis for the M3C2 distance comparison in the study area and the resulting calculation results.

projection scale [m]	**0.8783**
surface area [m²]	0.606
max depth [m]	**2.5**
Gauss mean [m]	-0.182
std. dev. [m]	0.194
RMS [m]	0.265

4.3 M3C2: Accuracy analysis by distance determination between M2-M17 with GCP and reference dataset M1

Fig. 8 shows the results from the unfiltered and filtered (conf) M3C2 distance determinations between M2-M17 and M1 using the optimized parameters shown in Table 8. In addition, the results of the M3C2 distance comparison are shown using the GCP and the parameters mentioned in Section 3.3.5.

a)

mission	flight mode	flight altitude [m]	GSD [cm/Pixel]	flight velocity [m/s]	camera tilt [°]	horizontal overlap [%]	vertical overlap [%]	shutter priority [s]	flight duration [min]	number of images [-]
M1	DG	50	1.37	3	60	60	80	no	51:45	950
M2	DG	50	1.37	3	60	60	80	no	51:45	950
M3	NG	50	1.37	3	60	60	80	no	29:14	536
M4	DG	80	2.19	4	60	60	80	no	21:58	337
M5	NG	80	2.19	4	60	60	80	no	14:00	214
M6	DG	110	3.01	4	60	60	80	no	21:04	244
M7	DG	110	3.01	4	60	60	80	no	15:20	173
M8	NG	110	3.01	4	60	60	80	no	10:05	112
M9	DG	110	3.01	4	90	60	80	no	10:50	122
M10	DG	110	3.01	8	60	60	80	1/1600	08:08	173
M11	NG	110	3.01	8	60	60	60	1/1600	05:18	58
M12	NG	110	3.01	4	90	60	80	no	09:54	110
M13	DG	110	3.01	8	90	60	80	1/1600	05:48	122
M14	NG	110	3.01	8	90	60	60	1/1600	05:10	57
M15	DG	110	3.01	4	90	60	60	no	10:44	64
M16	NG	110	3.01	4	60	60	60	no	10:04	59
M17	DG	110	3.01	4	60	60	60	no	15:24	90

b)

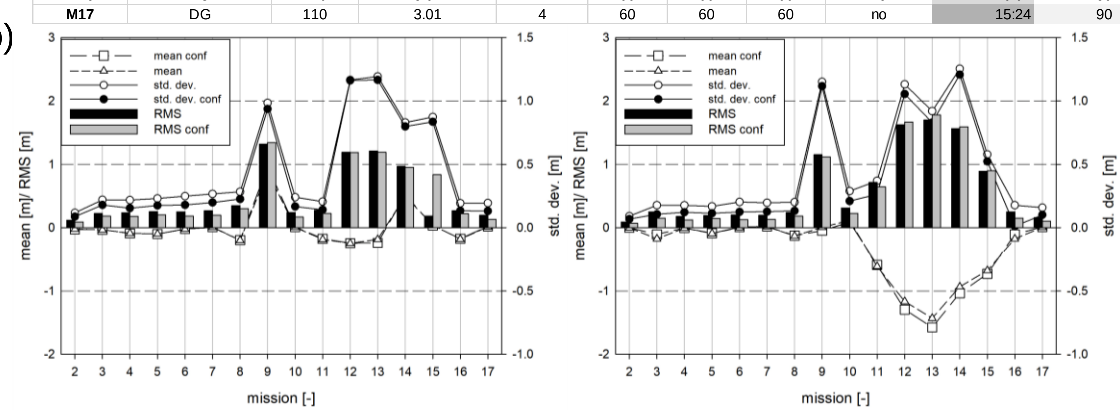

c)

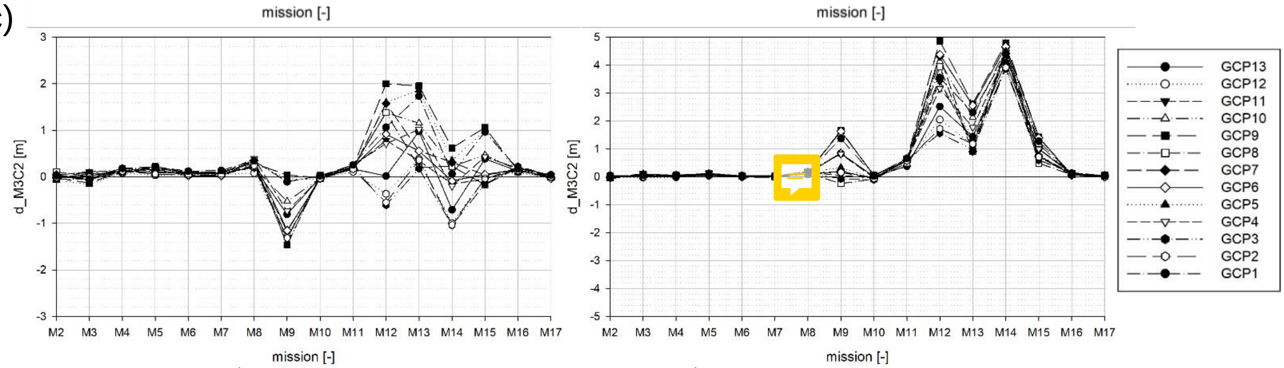

d)

mission	ΔGCP - survey 1: d_{mean}GCP - survey 1 [m]	ΔGCP - survey 1: d_{mean}GCP - survey 2 [m]	ΔM1 - survey 1, unfiltered: mean [m]	std.dev. [m]	RMS [m]	ΔM1 - survey 1, filtered: mean [m]	std.dev. [m]	RMS [m]	ΔM1 - survey 2, unfiltered: mean [m]	std.dev. [m]	RMS [m]	ΔM1 - survey 2, filtered: mean [m]	std.dev. [m]	RMS [m]
M1	-	-	-	-	-	-	-	-	-	-	-	-	-	-
M2	0.029	0.026	-0.022	0.117	0.119	-0.026	0.087	0.091	-0.003	0.091	0.091	-0.002	0.068	0.068
M3	0.062	0.060	-0.035	0.220	0.223	-0.031	0.179	0.182	-0.176	0.177	0.250	-0.107	0.106	0.151
M4	0.123	0.034	-0.087	0.218	0.235	-0.091	0.154	0.179	-0.006	0.176	0.176	-0.004	0.121	0.121
M5	0.154	0.091	-0.100	0.231	0.251	-0.099	0.175	0.201	-0.091	0.168	0.191	-0.088	0.113	0.143
M6	0.067	0.016	-0.024	0.248	0.250	-0.021	0.180	0.181	0.002	0.203	0.203	0.007	0.124	0.124
M7	0.072	0.020	0.005	0.266	0.266	0.007	0.198	0.198	0.014	0.196	0.197	0.019	0.127	0.128
M8	0.268	0.147	-0.201	0.283	0.347	-0.197	0.226	0.300	-0.131	0.201	0.240	-0.126	0.133	0.183
M9	0.877	0.648	0.876	0.985	1.318	0.963	0.937	1.344	0.005	1.152	1.152	-0.047	1.118	1.119
M10	0.026	0.046	0.005	0.240	0.240	0.012	0.167	0.167	0.114	0.289	0.310	0.087	0.210	0.227
M11	0.198	0.574	-0.186	0.205	0.277	-0.176	0.141	0.225	-0.611	0.370	0.714	-0.588	0.263	0.645
M12	0.997	3.315	-0.247	1.166	1.192	-0.245	1.163	1.188	-1.166	1.132	1.625	-1.294	1.055	1.670
M13	0.868	1.578	-0.185	1.194	1.209	-0.242	1.167	1.192	-1.431	0.921	1.702	-1.575	0.830	1.780
M14	0.463	4.353	0.498	0.830	0.968	0.520	0.799	0.953	-0.934	1.255	1.564	-1.035	1.208	1.591
M15	0.372	0.926	0.040	0.873	0.184	0.034	0.836	0.837	-0.678	0.578	0.891	-0.729	0.523	0.898
M16	0.155	0.100	-0.182	0.193	0.265	-0.175	0.134	0.220	-0.176	0.177	0.250	-0.107	0.106	0.151
M17	0.021	0.032	0.013	0.194	0.195	0.021	0.131	0.133	0.005	0.158	0.158	0.011	0.101	0.102

Fig. 8 a) Flight parameters of M1-M17 with the indication of the flight durations as well as the number of photos taken during the flight, b) mean value, standard deviation (std. dev.) and root mean square (RMS) resulting from M3C2 distance

computation between M2-M17 and the reference data set M1, c) mean value of the vertical distances between the GCP and the dense PC from M2-M17, d) values used in b) and c)

4.4 Change detection in the Laufer Muehle area

Fig. 9 illustrates the areas of significant change as a result of the CD for the data sets M2 (highest accuracy without using GCP) and M17 (the most effective parameter constellation in terms of recording time and accuracy, see section 5.4).

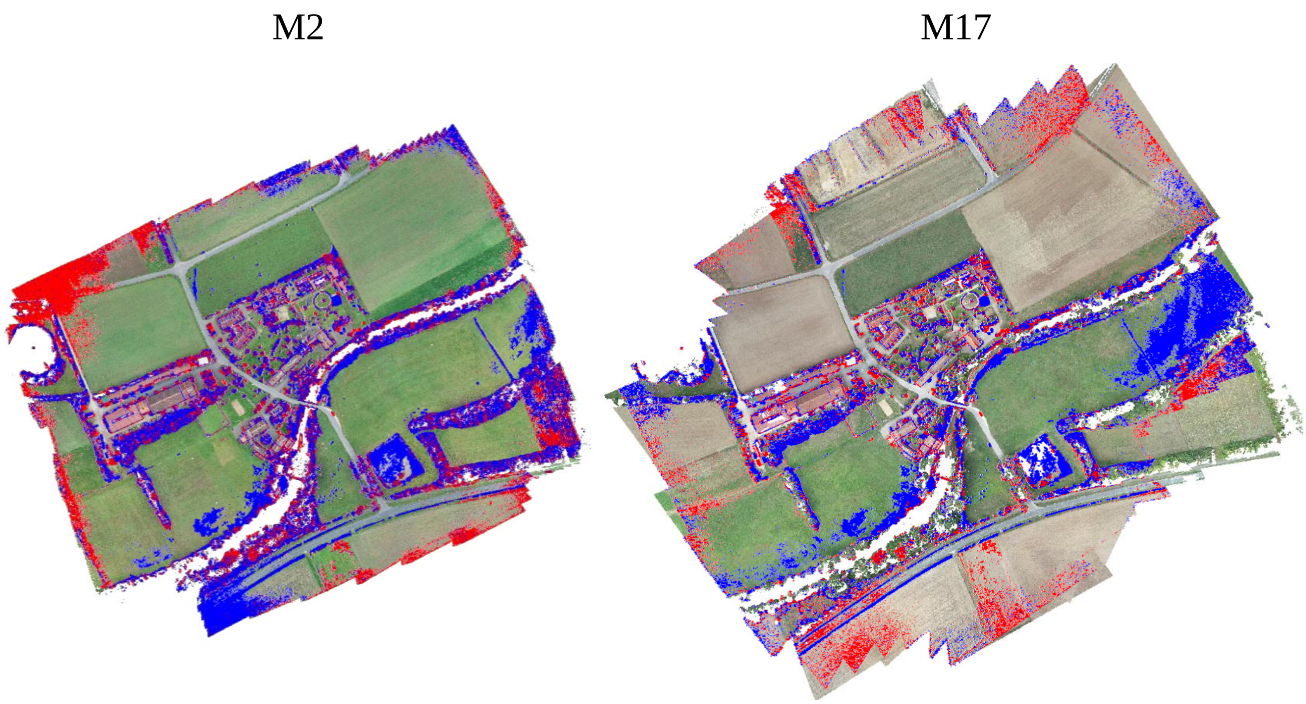

Fig. 9 Areas with detected changes between survey 1 and 2 of M2 and M17 in the Laufer Muehle area ($|d_{M3C2}| \geq 0.25\,m$; red: elevation increase in survey 2; blue: elevation decrease in survey 2)

Fig. 10 and **Fig. 11** show the changes in the study area in an anthropogenically influenced area. Based on the photos, the changes can be divided into the following categories:

1. debris pile - erosion
2. debris pile - accumulation
3. movable object
4. vegetation

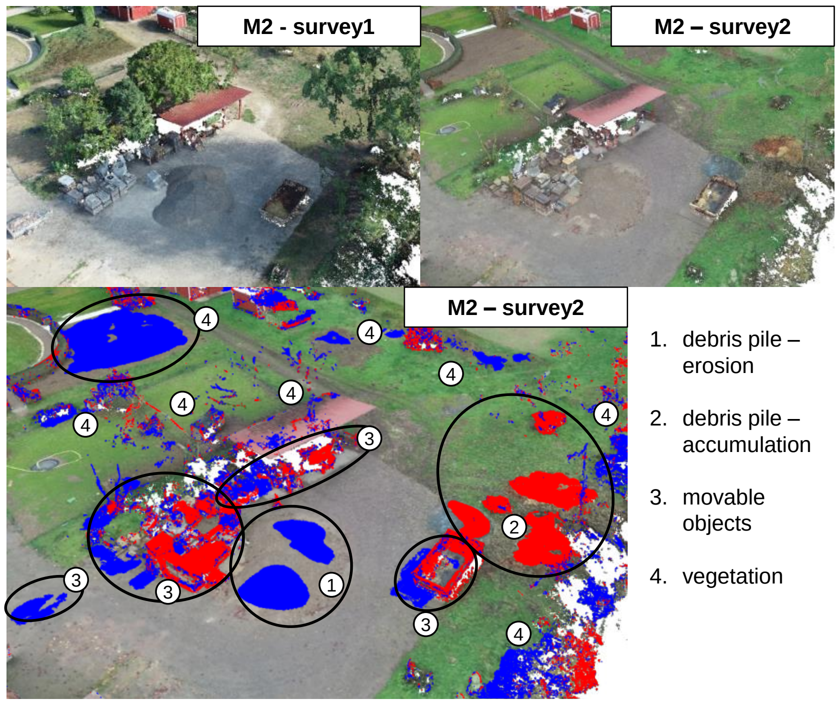

Fig. 10 PC (M2) from surveys 1 and 2 with the indication of CD ($|d_{M3C2}| \geq 0.25$ m; red: elevation increase in survey 2; blue: elevation decrease in survey 2)

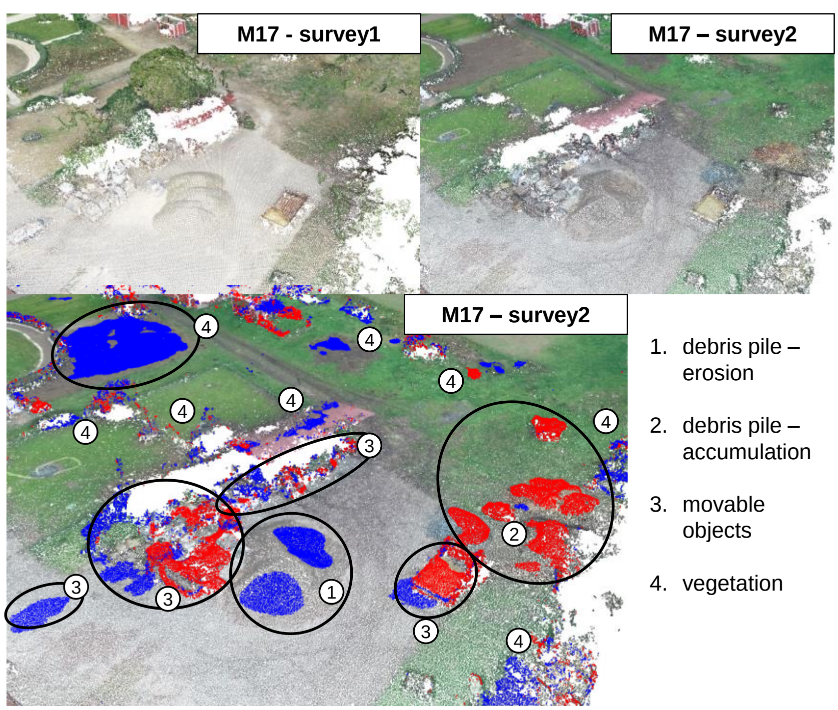

Fig. 11 PC (M17) from surveys 1 and 2 with color coding of CD ($|d_{M3C2}| \geq 0.25$ m; red: height increase in survey 2; blue: height decrease in survey 2)

It is conceivable that CD can be identified not only by comparison between data sets of the same mission. By determining the distance between survey 1 of mission i and survey 2 of another mission, differences in the multitemporal images can also potentially be identified. As an example, the difference between M1 survey 1 and M17 survey 2 is shown in **Fig. 12**.

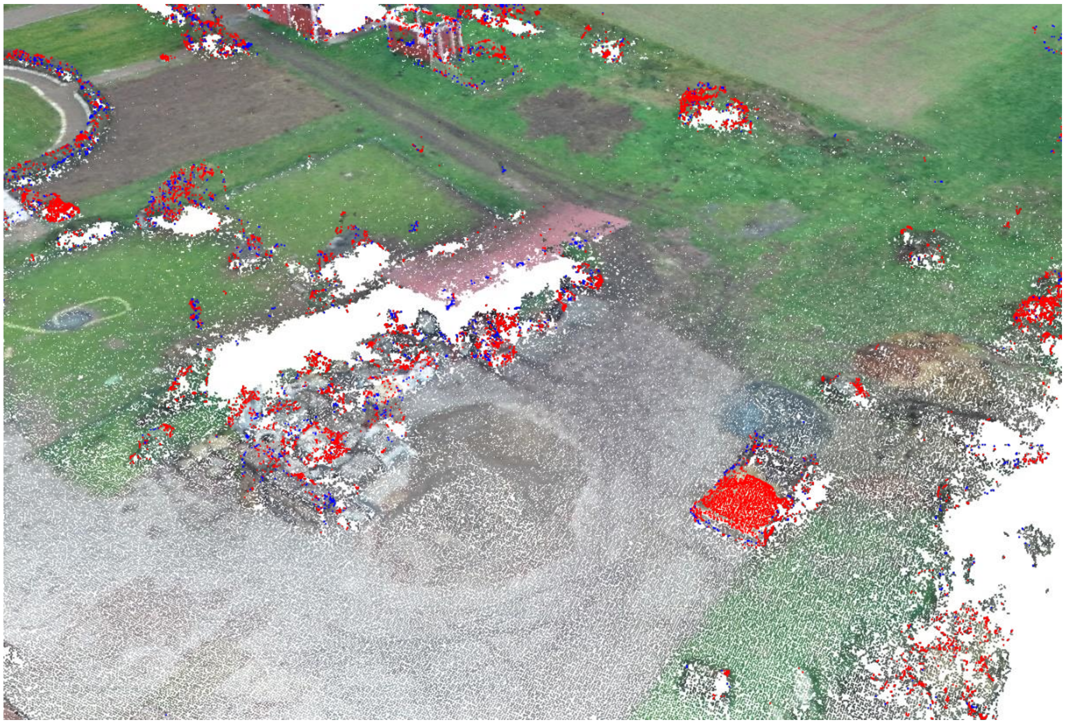

Fig. 12 CD between M2 survey 1 and M17 survey 2 ($|d_{M3C2}| \geq 0.25$ m; red: height increase in survey 2; blue: height decrease in survey 2)

5 Discussion

5.1 Comparison of the scope of the data between survey 1 and 2

The values presented in Table 7 show that in survey 1, although the same flight settings were used, the number of points resulting from each of the individual missions is always higher than in survey 2. In survey 1 (M1), a maximum of 21.8% of the points were filtered (M1), while in survey 2 (M14) up to 56.5 % of the points were filtered.

Particularly noteworthy is the number of points resulting from M10-M11 and M13-M14 in survey 2, which dropped significantly compared to the results from survey 1. Here, the recording results had deteriorated significantly, both in terms of quality and accuracy. This fact was also evident in the comparison and distance calculation with the reference dataset (Section 4.3).

5.2 Sensitivity analysis in the context of M3C2 distance determination

In the context of sensitivity analysis, **Fig. 7** shows that the RMS value increases significantly as max depth increases. The relationship of the increase between max depth and RMS corresponds approximately to a linear course. The mean value increases between max depth = 2.5 m and max depth = 12.5 m, then decreases again with max depth ≥ 12.5 m up to max depth = 25.0 m.

In the present observation, the influence of max depth in the M3C2 distance comparison on the accuracy seems to be pronounced.

Fig. 7 also shows that the increase of the projection scale also results in an increase of the (negative) mean distance between the two PC, but the RMS value is only slightly affected by this.

Due to the increase in error susceptibility with an increase in max depth shown in Fig. 7, a small value was consequently chosen for the data comparisons. To be able to identify larger changes in the study area, this value was not reduced further and was set to the smallest value examined (max depth = 2.5 m).

Although the influence of the projection scale on the error in the distance comparison according to Fig. 7 is relatively small, this parameter was determined based on the smallest corresponding RMS value for further investigations (projection scale = 0.8783). The subsequent M3C2 distance comparison with the optimized parameters yielded the desired result that the RMS value could be further reduced and was thus even lower than the smallest value determined up to this point, which meant a good parameter selection for the M3C2 distance determinations could be assumed.

~~5.3 Accuracy analysis of the calculation results from M2-M17~~

~~The analysis of the calculation results in Fig. 8 shows that the data resulting from a survey with nadir camera orientation (camera tilt = 90°, orientation perpendicular to the ground, used in M9 and M12-M15) have poor results related to distance determination. The mean value for M12-M15 was exclusively in the range of several decimeters and thus consequently in the range of poor results. The RMS and std. dev. values also confirmed the poor comparability of the data sets with the reference data set M1. The exception concerning the mean value was M9, where very good results were obtained for survey 2. The absolute values of both mean values exhibited very small deviations from the reference data set M1 (unfiltered: $|\text{mean}| < 0.005$ m; filtered: $|\text{mean}| < 0.047$ m;). However, the analysis of RMS and std. dev. as well as the corresponding normal distribution showed the importance of the complementary analysis of CD. In this context, **Fig. 13** shows an example~~

of the normal distribution using a sample with good (M2) and with poor (M9) distribution values. Especially in the case of the M9-values, the analysis of std. dev. and RMS shows significant deviations compared to the mean value.

All distribution functions presented can be found for all missions in Appendix 1.

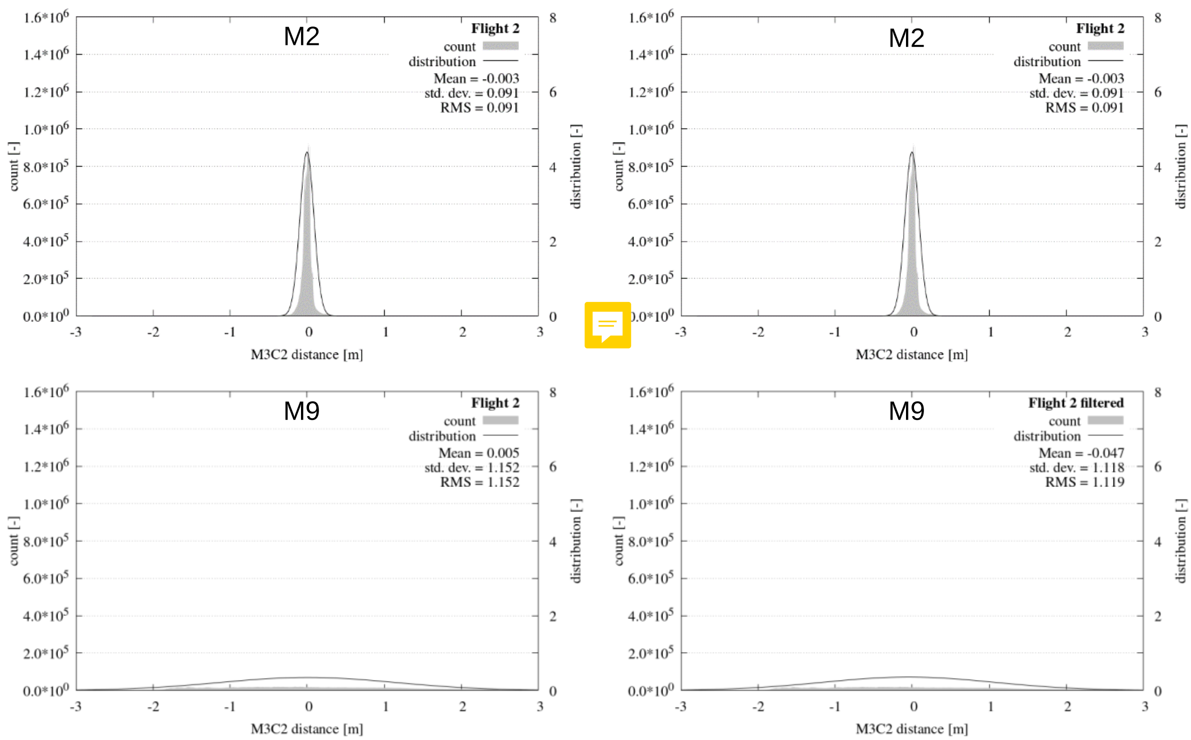

Fig. 13 Normal distributions and corresponding values from M3C2 distance determination with M1 using a positive (M2) and a negative (M9) example

5.4 Determination of suitable recording parameters for photogrammetric surveying in the Laufer Muehle area

The missions using a NG-flight mode led to worse results than the missions with a DG-flight mode concerning accuracy. An acceptable deviation from the reference data set could only be achieved by a low flight altitude, resulting in a long flight duration and a high number of images. Since these factors were to be kept as small as possible in the context of these investigations, the missions with NG-flight mode are to be classified as comparatively poor in comparison to the DG-flight mode missions.

After the exclusion of the missions based on the mentioned parameters (NG and 90° camera tilt) only the missions M2, M4, M6, M7, M10, and M17 remained, which showed acceptable accuracy values and could potentially be used within the framework of the planned investigations. In the context of near-real-time analyses, missions M2, M4, M6, and M7 are associated with a long flight duration and/or a high resulting number of images, which in turn leads to a high processing time for post-processing.

For the reasons mentioned above, missions M10 and M17 were chosen as the preferred variants for the flood investigations in the Laufer Muehle area.

With a flight duration of about 8 minutes, high-frequency recording intervals can be performed with the parameters from M10. The flight duration of approx. 15.5 minutes for M17 is comparatively high, but the number of images from M17 is comparatively low with 90 images (M10: 173 images).

Mission parameters in the case of a FE should therefore be selected in particular based on the required acquisition frequency. According to Fig. 8, the results from M17 yield better accuracies than those from M10, but M10 can produce higher frequency images. The total duration required for processing the photo images as part of the processing sequence shown in Fig. 6 could not yet be fully determined as part of these investigations. After this duration can be determined, an assessment of the recording capabilities of the M10 and M17 missions is possible and a final statement can be made on the selection of suitable survey parameters in the event of a flood event. Due to the higher accuracies, M17 is better suited for the identification of CD. Therefore, the results from M17 were focused on for the identification of CD in the further course of this research.

Analysis of CD results

Fig. 10 and Fig. 11 show that regarding vegetation, areas were identified where significant changes occurred between the two surveys. However, it was also noted that although data were filtered (by confidence value and by M3C2 distance) occurred, vegetation was still present as noise. Especially in the context of automated detection and categorization, which is an aim of this and further investigations, it is still necessary to develop further methods for filtering noise in this respect or to optimize the existing methods.

A comparison of Fig. 10 and Fig. 11 shows that both localization and extent of change were present to a very similar degree, and change could be similarly divided into different categories in both images. However, the PC with photorealistic coloring also shows a different level of detail in the surface structure, with M2 showing a better mapping of the surrounding area than M17.

In Fig. 9, changes in the study area are particularly apparent in areas with vegetation cover. In principle, the representation of changes in these areas is desirable, but since they are for the most part scattering points (noise), these points hardly indicate risk areas in the case of a FE. This again shows that further improvement of the methods is necessary to be able to achieve a suitable separation of CD due to noise and CD due to significant changes in the terrain.

Further changes can be seen at the edges of the PC. These areas are usually where the largest inaccuracies occur in SfM processes, so the changes identified there are negligible.

The comparison of the identified changes shown in Fig. 12 (M2 survey 1 - M17 survey 2) with the images in Fig. 10 and Fig. 11 shows that the localities of the changes are comparable. However, the identified changes in Fig. 12 are shown to a lesser extent. Also, some changes, such as mass redistribution in the debris pile area, were not detected.

In principle, the comparison between surveys from different missions may lead to good results in CD. Since good results were obtained in the analysis of CD at M17 and these also agreed with the high-resolution data set M2, no further investigations were carried out in this context.

6 Summary

For the photogrammetric analysis of flood events at the Aisch river using airborne imagery, investigations were carried out in the area of the Laufer Muehle. The area was to be imaged autonomously by an unmanned aerial vehicle (UAV) to determine and use an efficient flight parameter constellation (short flight duration with a low resulting number of images while maintaining sufficient accuracy within the results from Structure from Motion method (SfM)). This constellation should make it possible to image the study area at high frequency to detect changes in the terrain by multitemporal imaging (flood prevention) as well as to image the floodplains during a flood event (FE).

A total of 16 different flight parameter constellations (M2-M17) were investigated. For accuracy analysis as well as to create an optimized reference dataset, 13 GCP were located in the study area and georeferenced using a GPS rover with RTK connectivity. The photos were acquired using a Phantom 4 RTK unit. 3D-data sets were generated by photogrammetric reconstruction using Structure from Motion (SfM). The data with the presumably most accurate parameter constellation (M2) was optimized by including the georeferenced GCP in the SfM process. This optimization resulted in the M1 reference dataset. An M3C2 distance computation was performed between the results of the SfM process of M2-M17 and the georeferenced GCP, as well as the reference data set M1. Based on the analysis of normal distributions as well as different accuracy parameters (mean deviation, root mean square (RMS), standard deviation (std. dev.)), the results were evaluated based on their different recording parameters. Considering the accuracy values as well as the acquisition time and the number of images, two variants (M10 and M17) could be identified, which were considered suitable for CD acquisition before a FE, both in terms of time efficiency and accuracy aspects. Recording floodplains during a FE could not be investigated during this research due to a lack of data.

The final choice of the mission parameters depends on the desired time interval in which the area is to be imaged during a FE, with results from M17 achieving better accuracies compared to M10, but a shorter imaging interval can be achieved with M10. A conclusive statement about the total time required to analyze CD could not be made within the scope of these investigations.

Significant changes ($|d_{M3C2}| \geq 0.25\,m$) in the study area could be detected by the M3C2 distance calculation between the M2 survey 1 and M2 survey 2 (highest accuracy of the data) as well as between the M17 survey 1 and M17 survey 2 (most effective), using calculation parameters determined in a sensitivity analysis. The categorization of the changes could be done manually in a focus area of the study area due to the photorealistic coloring of the measurement points.

7 Future prospects

In these investigations, the M3C2 distance comparison with the reference data set M1 was carried out for all points of the data sets M2-M17. In the photogrammetric data sets, the edge areas of an investigation area are usually mapped much less accurately than the center area, since this area is covered by a large number of overlapping photos, while there are only a few photos available of the edge areas. If the distance calculations discussed in Section 3.3.6 were applied to a corresponding focal area without considering the edge areas, an improvement of the accuracy results discussed in Section 6.3 would be likely, especially in connection with the RMS and std. dev. values. Since this circumstance relates to all distance calculations performed, the evaluations of the individual missions performed in Section 5 remain valid.

To integrate the CD process into flood prevention, the data must be correlated with existing flood models. For this purpose, suitable interfaces have to be created, which allow a quick analysis in the study area in case of flood hazard. For this purpose, the identified changes have to be analyzed and categorized in more detail. In this way, it is possible to identify movable material that moves as float material in the event of a flood and can lead to damage or blockage of structures. In this context, the PC that are being compared need to be better cleaned of noise in order to optimize the M3C2 process.

These investigations were performed using relatively high SfM accuracy parameters, which may result in a correspondingly long processing time. The results obtained so far suggest that, in the context of plausible CD identification, these values should be considered a minimum. However, in the context of high-frequency recording of floodplains, it is conceivable that the analysis does not necessarily need to be performed using a PC, but that orthophotos can be used to estimate the two-dimensional location of floodplains. Since the accuracy studies conducted always referred to a 3D comparison, it cannot be excluded that the two-dimensional comparison (not considering the elevation component of the comparison vector) could lead to a good result for 2D localization. In this way, a significantly lower processing effort could be required within the SfM process. However, the possibilities in this context need to be determined in the context of a FE or tested on existing data from other investigations.

The flight parameter requirements determined within the scope of these investigations refer to the use of a Phantom 4 RTK UAV at a maximum flight altitude of 110 m and to the observation of an (in the case of a FE) relatively small observation area. Since FE usually have an impact on areas in the order of many square kilometers, it is necessary to investigate the scalability of the investigation results and possibly extend them to additional or different recording systems. A suitable approach is to compare the GSD, which is a measure of the resolution at which a survey area is mapped. With linear increases in flight altitude and camera resolution, the preservation of the accuracy statements made in this study is likely.

A disadvantage of the UAV measurement technique used in this research is that it cannot be used, or can only be used to a limited extent, during bad weather conditions (high wind speed, rain). Since these weather conditions usually accompany an FE, the approach proposed here is not fully applicable during an FE. Thus, it is necessary to extend the results of these investigations to the use of alternative aerial vehicle which can be operated during bad weather conditions.

The high-frequency representation of floodplains using orthophotos can lead to a good estimation of the development of the floodplain. To be able to determine a corresponding increase or decrease of the area, as well as the water depth resulting from the flooding, it is necessary to extract the water area from these data. Extensive research already exists for this purpose, which is often based on the use of AI-supported (artificial intelligence) technologies. Different deep learning methods for floodplain imaging are discussed, for example, in Bentivoglio et al. (2021), Gebrehiwot and Hashemi-Beni (2020), Hernández et al. (2022). The implementation of such systems is usually associated with a high effort and requires an extensive data basis for teaching the algorithm, which is why the feasibility of these methods for the Laufer Muehle study has to be determined in the course of further investigations.

8 Declaration

Funding The research was supported by the STAEDTLER foundation. The financial support included coverage of costs for travel, material/equipment, and personnel costs

Conflicts of interest/Competing interests

Not applicable

Availability of data and material

The datasets generated during and/or analyzed during the current study are available from the corresponding author upon reasonable request.

Code availability

Not applicable

Authors' contributions Michael Kögel contributed to the study conception and design, material preparation and data collection, data analysis, and creation of the manuscript. Dirk Carstensen contributed to the study conception and design, data evaluation and reviewing the draft. All authors approved this version to be published.

9 References

Agisoft LLC (2022a) Agisoft Metashape User Manual: Professional Edition, Version 1.8

Agisoft LLC (2022b) Metashape Python Reference: Release 1.8.4

Baltsavias EP (1999a) A comparison between photogrammetry and laser scanning. ISPRS Journal of Photogrammetry and Remote Sensing 54:83–94. https://doi.org/10.1016/S0924-2716(99)00014-3

Baltsavias EP (1999b) Airborne laser scanning: existing systems and firms and other resources. ISPRS Journal of Photogrammetry and Remote Sensing 54:164–198. https://doi.org/10.1016/S0924-2716(99)00016-7

Bayerische Staatskanzlei (2010) Anlage 1 BayWG - Verzeichnis der Gewässer erster Ordnung. https://www.gesetze-bayern.de/Content/Document/BayWG-ANL_1. Accessed 26 August 2022

Bayerisches Landesamt für Umwelt (2011) Entwurf einer kulturlandschaftlichen Gliederung Bayerns als Beitrag zur Biodiversität: 17 Aischgrund

Bayerisches Landesamt für Umwelt (2016) Verzeichnis der Bach- und Flussgebiete in Bayern: Flussgebiet Main. https://www.lfu.bayern.de/wasser/gewaesserverzeichnisse/doc/tab24.pdf#page=70. Accessed 25 August 2022

Bayerisches Landesamt für Umwelt (2022a) Angewandte Geologie: Ursprung der Aisch WSW von Illesheim. https://www.umweltatlas.bayern.de/mapapps/resources/reports/sb_geotope/generateBericht.pdf?additionallayerfieldvalue=575Q003

Bayerisches Landesamt für Umwelt (2022b) Gewässerkundlicher Dienst Bayern: Stammdaten Laufermühle. https://www.gkd.bayern.de/de/fluesse/wasserstand/bayern/laufermuehle-24263000. Accessed 24 August 2022

Bayerisches Landesamt für Umwelt (2023) Hochwassernachrichtendienst Bayern: Stammdaten Laufermühle / Aisch. https://www.hnd.bayern.de/pegel/regnitz/laufermuehle-24263000/stammdaten? Accessed 2 January 2023

Bentivoglio R, Isufi E, Jonkman SN, Taormina R (2021) Deep Learning Methods for Flood Mapping: A Review of Existing Applications and Future Research Directions

Cawood AJ, Bond CE, Howell JA, Butler RWH, Totake Y (2017) LiDAR, UAV or compass-clinometer? Accuracy, coverage and the effects on structural models. Journal of Structural Geology 98:67–82. https://doi.org/10.1016/j.jsg.2017.04.004

Dinkel A, Hoegner L, Emmert A, Raffl L, Stilla U (2020) Change detection in photogrammetric point clouds for monitoring of alpine, gravitational mass movements. ISPRS Ann. Photogramm. Remote Sens. Spatial Inf. Sci. V-2-2020:687–693. https://doi.org/10.5194/isprs-annals-V-2-2020-687-2020

DJI (2023) P4 RTK Techn. Daten. https://www.dji.com/de/phantom-4-rtk/info. Accessed 3 January 2023

El-Din Fawzy H (2019) 3D laser scanning and close-range photogrammetry for buildings documentation: A hybrid technique towards a better accuracy. Alexandria Engineering Journal 58:1191–1204. https://doi.org/10.1016/j.aej.2019.10.003

Eltner A, Hoffmeister D, Kaiser A, Karrasch P, Klingbeil L, Stöcker C, Rovere A (eds) (2022) UAVs for the environmental sciences: Methods and applications. wbg Academic, Darmstadt

Fischler MA, Bolles RC (1981) Random sample consensus. Commun. ACM 24:381–395. https://doi.org/10.1145/358669.358692

Forlani G, Dall’Asta E, Diotri F, Di Cella UM, Roncella R, Santise M (2018) Quality Assessment of DSMs Produced from UAV Flights Georeferenced with On-Board RTK Positioning. Remote Sensing 10:311. https://doi.org/10.3390/rs10020311

Gebrehiwot A, Hashemi-Beni L (2020) A Method to Generate Flood Maps in 3d Using dem and Deep Learning. Int. Arch. Photogramm. Remote Sens. Spatial Inf. Sci. XLIV-M-2-2020:25–28. https://doi.org/10.5194/isprs-archives-XLIV-M-2-2020-25-2020

Grussenmeyer P, Landes T, Voegtle T, Ringle K (2008) Comparison methods of terrestrial laser scanning, photogrammetry and tacheometry data for recording of cultural heritage buildings. The International Archives of the Photogrammetry, Remote Sensing and Spatial Information Sciences. Vol. XXXVII. Part B5. Beijing 2008

Hernández D, Cecilia JM, Cano J-C, Calafate CT (2022) Flood Detection Using Real-Time Image Segmentation from Unmanned Aerial Vehicles on Edge-Computing Platform. Remote Sensing 14:223. https://doi.org/10.3390/rs14010223

James MR, Robson S, Smith MW (2017) 3-D uncertainty-based topographic change detection with structure-from-motion photogrammetry: precision maps for ground control and directly georeferenced surveys. Earth Surf. Process. Landforms 42:1769–1788. https://doi.org/10.1002/esp.4125

Kögel M, Pflitsch A, Northup DE, Carstensen D, Medley JJ, Mansheim T, Killing T, Buschbacher M, Angerer H, Falkner J, Kynatidis A, Ott V, Regler S (2022) Combination of close-range and aerial photogrammetry with terrestrial laser scanning to answer microbiological and climatological questions in connection with lava caves. Appl Geomat. https://doi.org/10.1007/s12518-022-00459-7

Kutschera G, Blankenbach J, Blut C, Bolle F-W, Effkemann C, Gahlaut S, Hein N, Jagow M-L, Schüttrumpf H, Schwermann R, Tabatabaei S, Wöffler T (2018) Monitoring kleiner und mittlerer Fließgewässer mittels bemannter und unbemannter Wasserfahrzeuge – Ergebnisse des Projektes RiverView. Hydrologie und Wasserbewirtschaftung / BfG – Jahrgang: 62.2018,6 - ISSN 1439-1783. https://doi.org/10.5675/HyWa_2018.6_5

Lague D, Brodu N, Leroux J (2013) Accurate 3D comparison of complex topography with terrestrial laser scanner: Application to the Rangitikei canyon (N-Z). ISPRS Journal of Photogrammetry and Remote Sensing 82:10–26. https://doi.org/10.1016/j.isprsjprs.2013.04.009

Luhmann T (2013) Combination of Photogrammetry and Terrestrial Laserscanning – Potentials and Limitations, Part 2: Systems, Algorithms and Applications. Advances in Geodetic Sciences and Industry:81–90

Luhmann T (2018) Nahbereichsphotogrammetrie: Grundlagen - Methoden -Beispiele, 4th edn. Wichmann, Berlin, Offenbach

Mancini F, Salvini R (2020) Applications of Photogrammetry for Environmental Research. MDPI - Multidisciplinary Digital Publishing Institute

Marín-Buzón C, Pérez-Romero AM, León-Bonillo MJ, Martínez-Álvarez R, Mejías-García JC, Manzano-Agugliaro F (2021) Photogrammetry (SfM) vs. Terrestrial Laser Scanning (TLS) for Archaeological Excavations: Mosaic of Cantillana (Spain) as a Case Study. Applied Sciences 11:11994. https://doi.org/10.3390/app112411994

Meydenbauer A (1867) Die Photometrographie: Wochenblatt des Architektenvereins zu Berlin Jg. 1, 1867, Nr. 14, S. 125–126; Nr. 15, S. 139–140; Nr. 16, S. 149–150

Mora-Felix ZD, Sanhouse-Garcia AJ, Bustos-Terrones YA, Loaiza JG, Monjardin-Armenta SA, Rangel-Peraza JG (2020) Effect of photogrammetric RPAS flight parameters on plani-altimetric accuracy of DTM. Open Geosciences 12:1017–1035. https://doi.org/10.1515/geo-2020-0189

Mulsow C, Mandlburger G, Ressl C, Maas H-G (2019) Vergleich von Bathymetriedaten aus luftgestützter Laserscanner- und Kameraerfassung. Dreiländertagung der DGPF, der OVG und der SGPF in Wien, Österreich. Publikationen der DGPF

Nota EW, Nijland W, Haas T de (2022) Improving UAV-SfM time-series accuracy by co-alignment and contributions of ground control or RTK positioning. International Journal of Applied Earth Observation and Geoinformation 109:102772

OpenDroneMap (2022) OpenDroneMap. https://docs.opendronemap.org/

Przybilla H-J, Bäumker M (2020) Untersuchungen zur Qualität des Realtime Kinematic GNSS Systems der DJI Phantom 4 RTK: 40. Wissenschaftlich-Technische Jahrestagung der DGPF in Stuttgart. Publikationen der DGPF:47–61

Qin R, Tian J, Reinartz P (2016) 3D change detection – Approaches and applications. ISPRS Journal of Photogrammetry and Remote Sensing 122:41–56. https://doi.org/10.1016/j.isprsjprs.2016.09.013

Rusinkiewicz S, Levoy M (2001) Efficient variants of the ICP algorithm. In: Proceedings / Third International Conference on 3-D Digital Imaging and Modeling: 28 May - 1 June 2001, Quebec City, Canada. IEEE Computer Soc, LosAlamitos, Calif., pp 145–152

SAPOS (2015) Produktdefinition SAPOS. https://www.sapos.de/files/SAPOS-Produktdefinition_2017.pdf

Talha A, Fritsch D (2019) Integration of Laser Scanning and Photogrammetry in 3D4D Cultural Heritage: A review. IJAST 9:76–91

Triantafyllou A, Watlet A, Le Mouélic S, Camelbeeck T, Civet F, Kaufmann O, Quinif Y, Vandycke S (2019) 3-D digital outcrop model for analysis of brittle deformation and lithological mapping (Lorette cave, Belgium). Journal of Structural Geology 120:55–66. https://doi.org/10.1016/j.jsg.2019.01.001

Vosselman G, Maas H-G (eds) (2011) Airborne and terrestrial laser scanning. Whittles; CRC Press, Dunbeath, Boca Raton, Fla.

Waele J de, Fabbri S, Santagata T, Chiarini V, Columbu A, Pisani L (2018) Geomorphological and speleogenetical observations using terrestrial laser scanning and 3D photogrammetry in a gypsum cave (Emilia Romagna, N. Italy). Geomorphology 319:47–61. https://doi.org/10.1016/j.geomorph.2018.07.012

Wasserwirtschaftsamt Nürnberg (2021) Luftbilder HW2021

Wiggenhagen M, Steensen T (2021) Taschenbuch zur Photogrammetrie und Fernerkundung: = Guide for photogrammetry and remote sensing, 6th edn. Wichmann, Berlin, Offenbach

Winiwarter L, Anders K, Höfle B (2021) M3C2-EP: Pushing the limits of 3D topographic point cloud change detection by error propagation. ISPRS Journal of Photogrammetry and Remote Sensing 178:240–258. https://doi.org/10.1016/j.isprsjprs.2021.06.011

Xie H, Wang H, Yang Y, Chen Y, Yang J, Wang S, Liu Z (2021) Analysis of Underwater Topographic Survey of Stilling Basin Based on Unmanned Survey System. Advances in Materials Science and Engineering 2021:1–15. https://doi.org/10.1155/2021/5514165

Appendix 1

Click here to access/download
Supplementary Material
appendix-1_Koegel_eng.pdf